



This is to certify that the

Local Convection Heat Transfer thesis entitled coefficient For a two-dimensional wall jet with uniform Heat Flux presented by boundary Condition using Infrared imaging.

Ramez S. Abdul Nour

has been accepted towards fulfillment

of the requirements for

Master of Science Mechanical Eng.

Date 11/15/99



PLACE IN RETURN BOX to remove this checkout from your record.

TO AVOID FINES return on or before date due.

MAY BE RECALLED with earlier due date if requested.

DATE DUE	DATE DUE	DATE DUE

11/00 c/CIRC/DateDue.p65-p.14

LOCAL CONVECTION HEAT TRANSFER COEFFICIENT FOR A TWO DIMENSIONALWALL JET WITH UNIFORM HEAT FLUX BOUNDARY CONDITION USING INFRARED IMAGING

by

Ramez S. AbdulNour

A THESIS

Submitted to
Michigan State University
in partial fulfillment of the requirements
for the degree of

MASTER OF SCIENCE

Department of Mechanical Engineering

1999

ABSTRACT

LOCAL CONVECTION HEAT TRANSFER COEFFICIENT FOR A TWO DIMENSIONAL WALL JET WITH UNIFORM HEAT FLUX BOUNDARY CONDITION USING INFRARED IMAGING

by

Ramez S. Abdul Nour

The performance of automotive windshield defrosters is important for passenger safety and comfort. An experimental system was developed and used to generate benchmark data for a model heated wall jet flow using conditions relevant to automotive windshield defrosters as a means to aid defroster and defogger design.

The focus of this study was to measure the local heat transfer coefficient in the developing region of the wall jet with a uniform heat flux boundary condition. An infrared imaging system was used to measure the surface temperature field. The results were non-dimensionalized and compared to available literature data. The local convective heat transfer coefficient decreased rapidly from the jet exit plane to a minimum at approximately 4 jet slot widths (x/w), increased to a maximum at approximately x/w = 11.5 and then decreased. The local convection heat transfer coefficient, h_x , of the isoflux boundary condition was compared with that of an isothermal boundary condition using the same experimental system. The difference in h_x was largest at the leading edge of the heated wall and decreased in the streamwise direction.

To My Parents To All of My Siblings

ACKNOWLEDGEMENTS

I would like to take this opportunity to thank my parents, Sulaiman AbdulNour and Lydia Oussi, who believed in me and supported me throughout the years. I want to thank all of my older siblings for their encouragement and guidance to strive for higher goals. They always took the time to steer me into the right direction in life.

I would like to thank my major advisor Dr. McGrath and co-advisor Dr. Foss for their support during the two years at Michigan State and the two years after that. In addition, I would like to thank Dr. Somerton who never refused to help a student. Special thanks to the Mechanical Engineering Department staff at MSU for their help.

I would like to thank the engineering school staff at the University of Wyoming for their support and encouragement during my undergraduate education. My experience there was most valuable in developing the necessary engineering skills for the real world.

I would also like to thank all of my friends and colleagues who supported me throughout the years. I did not mention any names because there are so many of them and I would hate myself if I forget anyone. Finally, I want to say that the work presented here was only a small step in understanding the problem in hand. I hope that someone can carry on this work in future and learn from my mistakes.

TABLE OF CONTENTS

<u>Title</u>	Page
List of Tables	vii
List of Figures	viii
Nomenclature	xi
Chapter 1 - Introduction	1
1.1 Background and Literature Review	1
1.2 Objectives	5
Chapter 2 - Mathematical Models	7
2.1 Fundamental Heat Transfer Relationships	7
2.2 Non-Dimensional Heat Transfer Empirical Correlations	10
Chapter 3 - Experimental Methodology	13
3.1 Experimental Setup	13
3.1.1 Flow Facility	13
3.1.1.1 Slit Jet	14
3.1.1.2 Wall Section	14
3.1.2 Test Section for Uniform Heat Flux Boundary Condition	16
3.1.2.1 Core Assembly	17
3.1.2.2 Test Section	18
3.2 Instrumentation	23
3.2.1 Infrared Imaging Camera	23
3.2.2 Thermocouples	27

3.3 Uncertainty Analysis		28
Chapter 4 - Results and Discussion		31
4.1 Velocity I	4.1 Velocity Profiles	
4.2 Uniform I	Heat Flux Boundary Condition	35
4.2.1	Temperature Profiles	35
4.2.2	4.2.2 Local Convection Heat Transfer Coefficient	
	Non-Dimensional Local Convection Heat Transfer Coefficient	43
4.3 Local Convection Heat Transfer Coefficient for Isoflux and Isothermal Boundary Conditions		47
Chapter 5 - Conclusions and Recommendations		50
5.1 Conclusio	on ·	50
5.2 Recommendations		52
Appendices		
Appendix A	Conduction and Convection Heat Transfer Thermal Resistance Analysis	53
Appendix B	Calibration Curves and Data for Infrared Imaging and Thermocouple Measurement Techniques	56
Appendix C	Uncertainty Calculations of the Local Convection Heat Transfer Coefficient for the Isoflux Boundary Condition	66
Appendix D	Infrared Images of the Surface Temperature Distribution for the Isoflux Boundary Condition	76
List of References		80

Section 1

. •

Same Property of the Control of the

or y per 4 x € .

en programme de la companya de la co

4.7 4.74

•

LIST OF TABLES

<u>Tables</u>	<u>Title</u>	Page
Table 3.1	Uncertainty terms used to compute the total uncertainty in $h_{\!\scriptscriptstyle x}$ measurement.	29
Table 3.2	Estimated and measured percent uncertainties of the local convection heat transfer coefficient.	30
Table B.1	Freezing and boiling thermocouple calibration data.	63
Table C.1	Estimated uncertainty of the total energy term.	69
Table C.2	Estimated uncertainty of the conduction losses term.	70
Table C.3	Estimated uncertainty of the surface temperature using infrared camera measurements.	72
Table C.4	Estimated uncertainty of the surface temperature using thermocouple measurements.	73
Table C.5	Estimated uncertainty of the test section surface area.	74

LIST OF FIGURES

<u>Figures</u>	<u>Title</u>	Page
Figure 1.1	Wall jet velocity profile.	2
Figure 2.1	Wall jet profile and nomenclature of characteristic length and width.	10
Figure 3.1	Schematic of the flow facility.	14
Figure 3.2	Magnified view of the slit jet entrance region.	15
Figure 3.3	Detailed schematic of the plenum, knife edge and test section.	15
Figure 3.4	Wall and test section assembly.	16
Figure 3.5	Test section core assembly.	17
Figure 3.6	(a) Test section core assembly with insulation.(b) Test section core assembly with thermocouples attached on the back surface of the test section and inside the insulation.	19
Figure 3.7	Test section and electrical connections.	21
Figure 3.8	Magnified view of the top surface of the test section core assembly.	21
Figure 3.9	The infrared imaging camera and system used to acquire data.	24
Figure 3.10	(a) Schematic of the setup used to acquire the infrared thermal image.(b) Schematic of the setup used to capture the infrared thermal image for analysis.	25
Figure 4.1	(a) Mean velocity profiles in developing region [Willenborg, 1996].(b) Mean velocity profiles in self-preserved region [Willenborg, 1996].	32
Figure 4.2	Development of the characteristic jet width, δ_2 [Willenborg, 1996].	34
Figure 4.3	Maximum velocity decay behavior [Willenborg, 1996].	35

Figure 4.4	3-D infrared surface temperature contour with $q_{conv}^{H} = 1023 \text{ W/m}^2$ and $u_{ref} = 10 \text{ m/s}$.	36
Figure 4.5	2-D infrared surface temperature profile with $q_{conv}^n = 1023 \text{ W/m}^2$ and $u_{ref} = 10 \text{ m/s}$.	36
Figure 4.6	Temperature as a function of position using infrared camera and thermocouple data.	38
Figure 4.7	Non-dimensional temperature profile along the centerline of the heated test section for the isoflux case.	38
Figure 4.8	Thermocouple data of the front and back test sections.	39
Figure 4.9	Temperature warm up history of the test section using thermocouple data.	40
Figure 4.10	Temperature warm up history of the insulation using thermocouple data.	41
Figure 4.11	Temperature cool down history in the test section and insulation using thermocouple data.	41
Figure 4.12	Local convection heat transfer coefficient for the isoflux boundary condition.	42
Figure 4.13	Local convection heat transfer coefficient as a function of x_{ref}/w_{ref} for the isoflux boundary condition.	43
Figure 4.14	The non-dimensional local convection heat transfer coefficient using infrared camera data.	44
Figure 4.15	Comparison of the Local Minimum Non-dimensional Convection Heat Transfer Coefficient.	45
Figure 4.16	Comparison of present Nusselt number streamwise distribution with published data.	46
Figure 4.17	Comparison of the present Nusselt number with published empirical correlations.	47
Figure 4.18	The local convection heat transfer coefficient for isoflux and isothermal boundary conditions.	48
Figure 4.19	Percent variation of the local convection coefficient between the isothermal and isoflux boundary conditions.	49

Figure B.1	Infrared camera calibration curve for the 10° C temperature range. Other imaging parameters were: $T_{min} = 40^{\circ}$ C, $T_{max} = 50^{\circ}$ C, brightness level = 52 and contrast level = 72.	58
Figure B.2	Infrared camera calibration curve for the 20°C temperature range. Other imaging parameters were: $T_{min} = 35.1$ °C, $T_{max} = 55.1$ °C, brightness level = 52 and contrast level = 72.	59
Figure B.3	Infrared camera calibration curve for the 50° C temperature range. Other imaging parameters were: $T_{min} = 35.5^{\circ}$ C, $T_{max} = 85.5^{\circ}$ C, brightness level = 52 and contrast level = 72.	60
Figure B.4	Infrared camera calibration curve for the 10, 20 and 50°C temperature ranges. Other imaging parameters were similar to the ones reported in Figure B.1, 2, and 3.	61
Figure B.5	a) Thermocouple labels and locations on the back surface of the test section.	64
	b) Thermocouple labels and locations inside the insulation.	65
Figure D.1	2-D infrared surface temperature profile from test number a with $q_{conv}^{n} = 1023 \text{ W/m}^2$ and $u_{ref} = 10 \text{ m/s}$.	78
Figure D.2	2-D infrared surface temperature profile from test number c with $q''_{conv} = 1023 \text{ W/m}^2$ and $u_{ref} = 10 \text{ m/s}$.	78
Figure D.3	2-D infrared surface temperature profile from test number d with $q''_{conv} = 1023 \text{ W/m}^2$ and $u_{ref} = 10 \text{ m/s}$.	79
Figure D.4	2-D infrared surface temperature profile from test number e with $q_{conv}^n = 1023 \text{ W/m}^2$ and $u_{ref} = 10 \text{ m/s}$.	7 9

NOMENCLATURE

A = test section surface area, m^2 .

g = acceleration of gravity at sea level $= 9.81 \text{ m/s}^2$.

Gr_L = non-dimensional ratio of buoyancy to viscous forces.

h_x = local convection heat transfer coefficient, W/mK.

I = electrical current applied to the test section, amps.

k = thermal conductivity of air, W/m^2K .

 k_{ins} = thermal conductivity of the thermal insulation, W/m²K.

L = test section length, m.

 $Nu_{ref} = non-dimensional convection heat transfer coefficient = <math>h_x w_{ref}/k$.

 q''_{cond} = conduction heat flux loss, W/m².

 q''_{conv} = convection heat flux loss, W/m².

 q_{rad} = radiation heat flux loss, W/m^2 .

q"total = total electrical flux supplied to the system, W/m².

 P_{pl} = plenum pressure, Pa.

P_{amb} = ambient pressure in the flow facility, Pa.

R = electrical resistance of the test section, ohms.

Re_e = exit Reynolds number $\equiv u_e w/v$.

 $Re_L = length Reynolds number \equiv u_o L/v.$

 Re_{ref} = reference Reynolds number = $u_{ref}w_{ref}/v$.

 T_{amb} = ambient temperature in the flow facility, °C.

 T_{ins} = temperature in the center of the thermal insulation, °C.

 T_i = air jet temperature, °C.

 T_s = local test section surface temperature, °C.

 $T_{s,ave}$ = average test section surface temperature, °C.

u = local velocity, m/s.

- u_e = average velocity at the jet exit = (volume flow rate)/(jet exit area), m/s.
- u_j = inviscid core velocity = $[2 (P_{pl} P_{amb})/\rho]^{1/2}$, m/s.
- $u_m = maximum local velocity, m/s.$
- $u_{ref} = u_{ve}$ for this study and u_e for published literature, m/s.
- u_{ve} = average velocity at the vena contracta
 ≡ (volume flow rate at the vena contracta)/(jet area at the vena contract), m/s.
- V = electrical voltage applied across the test section, volts.
- w = width of the jet nozzle exit, m.
- $w_{ref} = w_{ve}$ for this study and w for published literature, m.
- w_{vc} = width of the jet at the vena contracta, m.
- x = streamwise distance from the jet exit plane, m.
- $x_{ref} = x_{vc}$ for this study and x for published literature, m.
- x_{vc} = streamwise distance from the vena contracta, m.
- x^* = streamwise distance to account for the virtual origin ($x^* = x + x_0$), m.
- x_0 = streamwise distance from the virtual origin to the jet exit plane, m.
- y = distance perpendicular to the wall, m.
- y_{ins} = distance from the surface of the test section to the center of the insulation, m.
- β = expansion coefficient, K^{-1} .
- δ_2 = distance normal to the wall in the outer layer where u/u_m = 0.5, m.
- ε = emissivity of the test section surface.
- $v = \text{kinematic viscosity, m}^2/\text{s.}$
- θ = non-dimensional temperature $\equiv (T_s T_j)/(T_{s,ave} T_j)$.
- ρ = density of air, kg/m³.
- σ = Stephan-Boltzman constant = 5.67 x 10⁻⁸ W/m²K².

CHAPTER 1

INTRODUCTION

1.1 Background and Literature Review

Wall jets have been studied by many investigators in the past due to their applications in a wide range of technological fields. These applications include automotive air conditioning (A/C) systems, industrial furnaces, and forces applied to airplanes during take off. The current study was motivated by the design of automotive A/C systems. Wall jets are a dominant type of flow field leaving the windshield defroster. The wall jet profile is what controls the heat transfer mechanism between the defroster air and the windshield. Therefore, a fundamental understanding of the wall jet fluid mechanics and heat transfer characteristics can lead to better A/C system design.

The first experimental study of wall jets was carried out by Forthmann in 1934 [Launder and Rodi, 1981]. However, it was not until the early 1960's that more wall jets studies were performed. Only a few of those studies were reviewed in this report based on their

relevance to the hydrodynamic and heat transfer work pertaining to this research. This study focused on evaluating the heat transfer properties of the wall jet immediately downstream of the nozzle exit where the wall jet characteristics are greatly influenced by the nozzle geometry upstream of the nozzle exit [Panton, 1984]. The present study examined a region where the nozzle exit geometry effect starts diminishing which is the region of major focus for most previous investigations.

A typical wall jet velocity profile is shown in Figure 1.1. A wall jet consists of two flow regions. The first region is a shear or boundary layer flow along the wall and it extends from the wall to the location of the maximum velocity, u_m . The second region is similar to a free jet flow and it extends from the maximum velocity to the edge of the free jet.

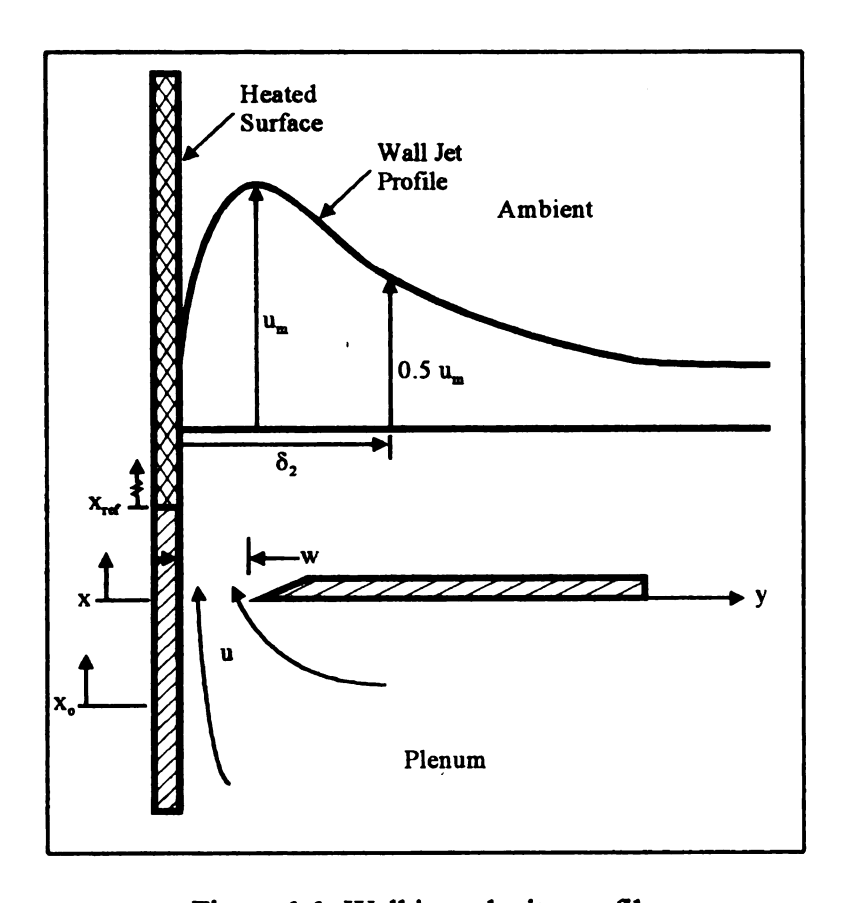


Figure 1.1. Wall jet velocity profile.

Sigalla provided a review of wall jet studies up to 1958 [Sigalla, 1958]. The work he presented was for fully turbulent wall jets, which started at approximately 20 nozzle widths, w, downstream of the jet exit. He described the decay of the maximum velocity as a function of the characteristic non-dimensional length, x/w, using the following correlation:

$$u_m/u_j \propto (x/w)^{-1/2}$$

A study by Akfirat determined the local heat transfer coefficient, h_x , of a 2-D wall jet with an isothermal boundary condition from upstream of the nozzle exit to x/w = 80 [Akfirat, 1966]. The jet exit plane Reynolds number, Re_e , for his study ranged from 190 to 16,620 and the leading edge of the test section was placed upstream of the nozzle exit. The study showed that the local convection heat transfer coefficient displayed a minimum value shortly downstream of the nozzle exit and a maximum farther downstream. The location of the minimum and maximum h_x was dependent on the nozzle geometry. However, the location of the maximum h_x was independent of the Re_e . For $Re_e > 1000$, it was found that the heat transfer rates are greatly influenced by the average exit velocity, u_e , and the discharge conditions for the 0 < x/w < 4 region where a laminar boundary layer exists. In other words, the exit velocity and the discharge conditions have a large influence on the wall jet for small x/w and less influence for large x/w. Finally, he showed that the nozzle exit width, w_x , influenced the magnitude and distribution of h_x for x/w > 10.

Mabuchi and Kumada used a mass transfer analogy to derive heat transfer relations for turbulent wall jets [Mabuchi and Kumada, 1972]. They experimentally studied the effect

of the boundary layer development in the jet nozzle region on the heat transfer in the developing wall region. Again, they demonstrated that the velocity profile is dependent on the nozzle geometry in the developing region. They presented the decay of the maximum velocity in a fashion similar to Sigalla:

$$u_{\rm m}/u_{\rm j} \propto (x^*/w)^{-0.525}$$

It should be noted that the virtual length, x^* , was used instead of x as in the Sigalla correlation. The virtual length was defined as the streamwise distance from the virtual origin of the jet upstream of the nozzle exit plane to the nozzle exit plane. The virtual length was used because it is independent of the exit Reynolds number. Their heat transfer data exhibited the same pattern as Akfirat's data in terms of the location of the minimum and maximum h_x .

Nizou studied the heat transfer coefficient of a turbulent wall jet using an isothermal boundary condition [Nizou, 1981]. The leading edge of the heated surface was located at the nozzle exit. Three different nozzle widths and an exit Re_e ranging from 9,000 to 60,000 were examined. All measurements were in the fully developed region (x/w > 30) and, hence, they were independent of the local discharge conditions.

A review paper published by Launder and Rodi for 2-D turbulent wall jets provided comprehensive data describing previous studies of 2-D turbulent wall jets [Launder and Rodi, 1981]. These studies were only concerned with the fluid mechanics of wall jets.

They demonstrated the self-similarity characteristic of the wall jet for flow fields similar to the one used in this study. Also, the rate of the maximum wall jet decay was presented

as a function of the location in the streamwise direction.

1.2 Objectives

The purpose of this study was to establish benchmark data to aid in the design and development of automotive A/C systems. These data will be used to validate the computational fluid dynamics (CFD) models employed in the design of automotive A/C systems. Therefore, it was important to create a relatively simple experimental study that could be duplicated using CFD modeling.

The actual wall jet in a car is a three dimensional impinging jet with an ill-defined thermal boundary condition. This study was the first phase to simulate the actual windshield defroster. The focus of this research was on a two-dimensional wall jet with a well-defined thermal boundary condition. Additionally, locations close to the jet inlet are relevant to windshield defroster design.

The work presented here was part of an effort to measure the heat transfer coefficient for both isothermal and isoflux boundary conditions. In accordance with flat plate flow, it was hypothesized that the heat transfer coefficient for both boundary conditions would be practically the same for a turbulent flow. Therefore the main objective of the overall study was to determine how sensitive the local convection heat transfer coefficient was to the two distinctly different thermal boundary conditions, isothermal and isoflux. This is important for CFD modeling because it is capable of simulating either the isothermal or isoflux boundary condition relatively more reliably than the conjugate heat transfer

boundary condition. Therefore, if the above hypothesis is true, then the CFD modeling can specify either isothermal or isoflux boundary condition. In addition, the isoflux boundary condition can provide more comprehensive experimental heat transfer data and it requires considerably less time to obtain the data than the isothermal boundary condition.

The overall study was divided into two parts; isoflux boundary condition and isothermal boundary condition. This report will only discuss the details of the isoflux boundary condition. The present study focused on the development and application of an experimental facility for quantifying the local convection heat transfer coefficient using an isoflux thermal boundary condition.

The objectives of this study can be summarized as follows:

- Develop an experimental setup using infrared imaging to obtain reliable h_x
 measurements. The setup was also designed to allow future modifications to allow 3-D impinging jet measurements.
- 2. Provide benchmark data for CFD modeling development for A/C systems.
- Obtain local convection heat transfer coefficient measurements of a wall jet using isoflux boundary conditions for x_{ref}/w_{ref} < 20.

CHAPTER 2

MATHEMATICAL MODELS

2.1 Fundamental Heat Transfer Relationships

The local heat transfer convection coefficient for the uniform heat flux boundary condition was computed using:

$$h_x = \frac{q_{conv}}{(T_s - T_j)} \tag{2.1}$$

where q_{conv} is the surface convection heat flux, T_s is the surface temperature, and T_j is the air jet temperature. The uniform heat flux boundary condition was achieved by applying an electrical current to a test section with uniform electrical resistivity. The uniform convection heat flux was computed using:

$$q_{conv} = q_{total} - q_{cond} - q_{red}$$
 (2.2)

where q total is the total electrical flux applied to the test section, q cond and q are the heat fluxes lost to the surroundings by means of conduction and radiation heat transfer, respectively.

The total electrical flux was computed using:

$$q_{total} = \frac{I^2 R}{A} = \frac{I V}{A}$$
 (2.3)

where I is the electrical current applied to the test section, R is the electrical resistance of the test section, V is the electrical voltage across the test section, and A is the surface area of the test section.

The test section was insulated using fiber glass thermal insulation as will be described in the experimental methodology chapter. The conduction heat loss through the insulation was computed using the following 1-D conduction model:

$$q_{cond} = -k_{ins} \frac{\partial T}{\partial v}$$
 (2.4)

where k_{ins} is the thermal conductivity of the insulation and $\partial T/\partial y$ is the 1-D temperature gradient from the front surface of the test section where the energy was applied toward the center of the insulation. Eq. 2.4 was evaluated for the steady state condition using:

$$q_{\text{cond}} = -k_{\text{ins}} \frac{\Delta T}{\Delta y} = -k_{\text{ins}} \frac{\left(T_{\text{s}} - T_{\text{ins}}\right)}{y_{\text{ins}}}$$
(2.5)

where T_s is the local surface temperature of the test section, T_{ins} is the temperature inside the thermal insulation, and y_{ins} is the distance from the test section surface to the thermocouple location inside the insulation. The term $\Delta T/\Delta y$ was evaluated using thermocouple measurements of T_s , and T_{ins} that were located at the same streamwise location.

The radiation heat loss was computed using the classical radiation model:

$$q_{rad}^* = \varepsilon \, \sigma \left(T_{s,ave}^4 - T_{amb}^4 \right) \tag{2.6}$$

where ε is the emissivity of the surface absorbing or emitting the radiation, σ is the Stephan-Boltzmann constant, $T_{s,ave}$ is the average test section surface temperature, and T_{amb} is the test facility ambient temperature. Eq. 2.6 assumes that the test section could be approximated as a black body with a view factor of one because the test section was much smaller than the surroundings. The procedure used to determine ε will be described later in the experimental methodology chapter.

Natural convection effects were evaluated using the classical approach of computing the ratio of the buoyancy to the inertial forces. The ratio is expressed as:

$$\frac{Gr_L}{Re_r^2} \tag{2.7}$$

where the Reynolds number, ReL, is expressed as:

$$Re_{L} = \frac{u_{e}L}{v}$$
 (2.8)

and the Grashof number, GrL, is expressed as:

$$Gr_{L} = \frac{g\beta(T_{s,ave} - T_{amb})L^{3}}{V^{2}}$$
 (2.9)

where u_e is the average exit jet velocity, β is the expansion coefficient, g is the acceleration of gravity, T_{amb} is the test facility ambient temperature, L is the test section streamwise length, and v is the viscosity of air. Evaluation of Eq. 2.7 showed that the buoyancy forces were negligible with respect to the inertial forces for the average velocity used in this study. Therefore natural convection effects were neglected.

2.2 Non-Dimensional Heat Transfer Empirical Correlations

Several non-dimensional heat transfer correlations have been presented by previous investigators in terms of the Nusselt and Reynolds numbers. These correlations were presented in the following form:

$$Nu_{ref} = C Re_{ref}^{0.8} \left(\frac{x_{ref}}{w_{ref}} \right)^{-0.6}$$
 (2.10)

where C is a constant ranging from 0.071 to 0.115 (Akfirat, 1966, Mabuchi and Kumada, 1972, and Sigalla, 1958). The definition of x_{ref} and w_{ref} is illustrated in Figure 2.1 and will be discussed below. Sigalla arrived at this correlation using skin friction measurements, while Mabuchi and Kumada used mass transfer data to obtain the heat transfer data by analogy. Only Akfirat used direct temperature measurements to obtain heat transfer data. The reference Nusselt and Reynolds numbers are defined as:

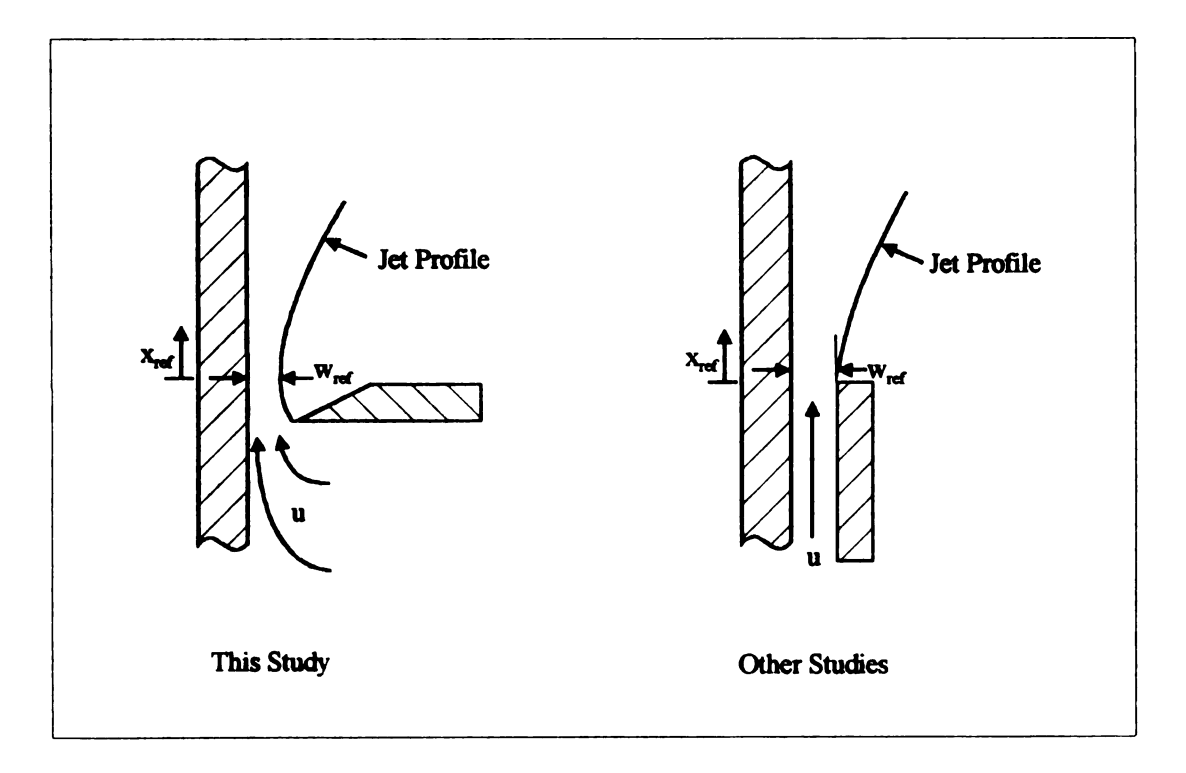


Figure 2.1 Wall jet profile and nomenclature of characteristic length and width.

$$Nu_{ref} = \frac{h_x w_{ref}}{k}$$
 (2.11)

and

$$Re_{rof} = \frac{u_{rof} w_{ref}}{v}$$
 (2.12)

The choice of the reference velocity and width are dependent on the nozzle geometry used in the previous and present studies. Previous investigations used a contour nozzle in comparison to the knife edge nozzle used in this study (see Figure 2.1). The knife edge slit jet was used because the velocity field exiting from the nozzle is characterized by a thin boundary layer and, therefore, the flow is insensitive to the magnitude of the exit Reynolds number [Ali and Foss, 1990]. All studies reviewed here defined the reference velocity, u_{ref} , as the average jet velocity at the nozzle exit, x_{ref} as the local streamwise distance starting at the nozzle exit, and w_{ref} as the jet width at the nozzle exit. However, the results presented in this work will define u_{ref} as the average jet velocity at the vena contracta, x_{ref} as the local streamwise distance starting at the vena contracta, and w_{ref} as the jet width at the vena contracta. The vena contracta was chosen as the reference location in this study because the jet profile there was more similar to the jet profile at the nozzle exit for previously reported studies. Therefore, the leading edge of the thermally active test section was located at the vena contracta.

The jet core velocity was calculated using the Bernoulli equation:

$$u_{j} = \sqrt{\frac{2(P_{pl} - P_{amb})}{\rho}}$$
 (2.13)

where P_{pl} is the plenum pressure and P_{amb} is the ambient pressure inside the test facility (see Figure 1.1). The flow field for this study was generated by a pressure difference across the slit jet as discussed in the experimental methodology chapter. The pressure drop measurement across the plenum was used to compute the volume flow rate through the plenum using a previously established system resistance curve [Foss, 1996]. The average jet exit velocity was calculated using:

$$u_e = \frac{\text{Volume Flow Rate}}{\text{Jet Exit Area}}$$
 (2.14)

Finally, the temperature data were presented in a non-dimensional form using:

$$\theta = \frac{(T_i - T_j)}{(T_{s,svo} - T_j)} \tag{2.15}$$

This non-dimensionalization scheme was chosen because it eliminated the bias error inherent in the measurement as will be made clear in the Results and Discussion chapter.

CHAPTER 3

EXPERIMENTAL METHODOLOGY

3.1 Experimental Setup

3.1.1 Flow Facility

A schematic of the flow facility used for this study is shown in Figure 3.1. The facility was part of the Turbulent Shear Flows Laboratory at Michigan State University. It consisted of a plenum, a discharge slot for the flow entering the receiver where the test section was located, and a flow control valve which provided manual control of the flow leaving the facility. Precautions were taken to insure a uniform velocity field passing through the slit jet, which was the inlet into the test section. The plenum was equipped with flow filters and three -40 mesh screens to minimize any disturbances in the flow entering the receiver. The average inlet velocity was determined by measuring the differential pressure between the plenum and the receiver and applying the Bernoulli equation. The differential pressure was measured using a 1 Torr MKS Baratron pressure transducer with a resolution of \pm 0.08% of the measured value [MKS Instrument, Inc]. A rubber seal was added to the

interface between the plenum and the slit jet assembly to eliminate any air leakage from the plenum into the chamber without passing through the test section. The entire flow facility was sealed to eliminate air leakage from the outside ambient into the receiver.

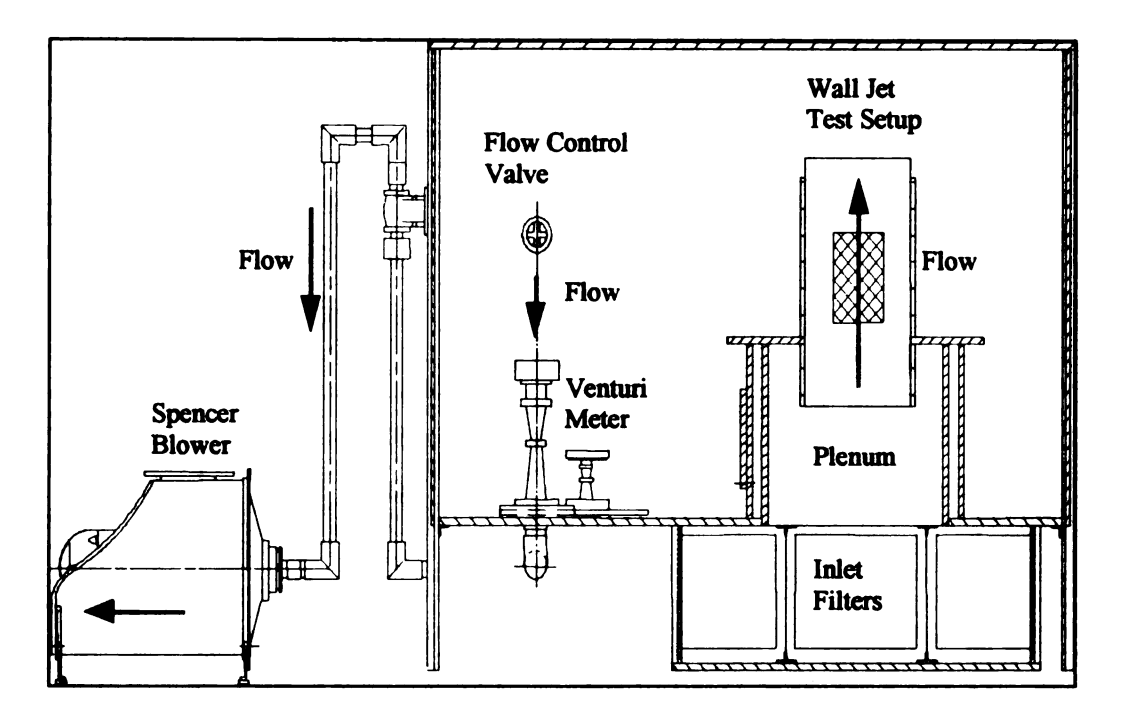


Figure 3.1. Schematic of the flow facility.

3.1.1.1 Slit Jet

The slit jet was constructed using two aluminum knife edges (see Figure 3.2). Two slots on each side of the knife edge were used to attach the knife edge to the structure covering the plenum. The slots were used to adjust the knife edges to the desired slit jet width. The slit jet width was set using precisely machined gauge blocks.

3.1.1.2 Wall Section

The wall was constructed using smooth double-sided plywood. A schematic of the wall section and the slit jet assembly is shown in Figure 3.3. The wall section extended into the

plenum by a distance of 8 slot widths (x/w) to insure the two-dimensionality of the jet.

Rails were constructed in the central portion of the wall to allow the test section to slide in and out as shown in Figure 3.4. The upper sliding portion of the wall had two holes to

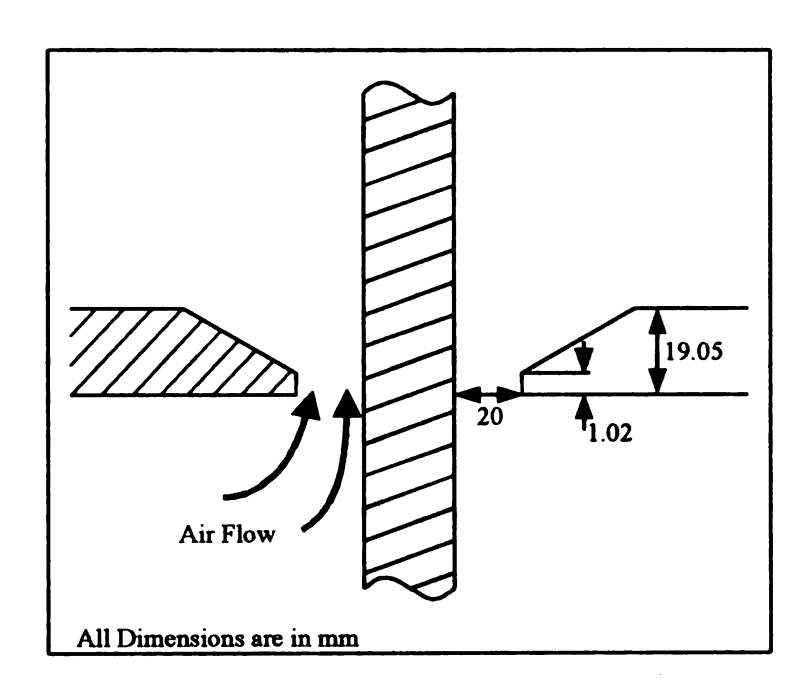


Figure 3.2. Magnified view of the slit jet entrance region.

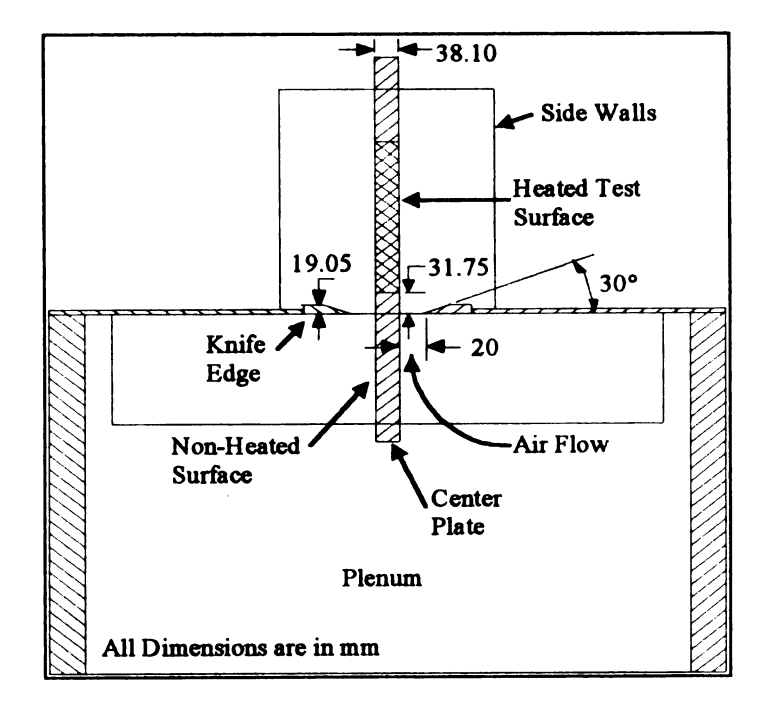


Figure 3.3. Detailed schematic of the plenum, knife edge and test section.

allow the instrumentation wires to pass through to the analog to digital (A/D) board.

Angle iron side supports were used to anchor the wall in place and to provide support to keep it from vibrating. The side supports were fabricated to allow for movement in the vertical direction. Side walls were extended inside the plenum to insure two-dimensionality of the jet (see Figure 3.3). The walls extended by a distance of 6.5 slot widths into the plenum.

3.1.2 Test Section for Uniform Heat Flux Boundary Condition

Symmetry was used to create the thermal and hydrodynamic boundary conditions as shown in Figure 3.3. Thermal symmetry was achieved by using two test sections, one on each side of the wall. Figure 3.4 shows a test section that was attached to the core assembly. The assembly was then inserted into the main wall section. Details of the test



Figure 3.4. Wall and test section assembly.

section assembly will be described in the following section. Surface temperature profiles were obtained using an infrared (IR) camera facing the front side of the wall only.

However, symmetry was verified using thermocouples that were attached at the same locations on the front and back test sections.

3.1.2.1 Core Assembly

The core of the test section was a hollow chamber fabricated out of ren-shapeTM composite wood [Ciba-Geigy Tooling] (see Figure 3.5). This specialty wood provided precise machining capability and thermal conductivity similar to the wall section. The top surface of the chamber included two holes to allow all the instrumentation wires to pass through it. The inside of the chamber was filled with fiber glass thermal insulation the same as the industrial piping insulation. The insulation had an estimated conductivity of



Figure 3.5. Test section core assembly.



0.038 W/mK [Incropera and DeWitt, 1990]. Thermocouples were attached to the surface between the chamber walls and the insulation to monitor chamber heating during the tests. Using a wooden column, thermocouples were also mounted inside the insulation itself to monitor the heating in the insulation and to help compute heat conduction losses (see Figure 3.6). The depth of the core plus the two test sections was matched to the wall section to avoid disturbances to the hydrodynamic boundary layer.

3.1.2.2 Test Section

The test section was 25.4 cm long and 17.8 cm wide. Two different techniques were used to fabricate the test section. Both techniques were based on using a substrate coated with a thin layer of Indium Tin Oxide (ITO) [Applied Films Corporation, 1993]. The ITO film was electrically resistive and it was meant to generate a uniform heat flux when passing an electrical current through it. This type of test section was attractive because the substrate provided a relatively high thermal resistance to conduction heat transfer and prevented heat smearing effects in the axial direction (see Appendix A for thermal resistance calculations). In addition, the ITO coating provided a reasonable maximum current to realize the desired isoflux boundary condition.

Several configurations were evaluated. The first technique used a plastic substrate coated with ITO film. The plastic substrate was attached to a glass surface using low viscosity glue. The glue was applied between the glass and the substrate in a careful rolling motion to prevent the entrapment of air bubbles. Then the glue was cured using either ultra violet light or a bright yellow light source.



Figure 3.6. (a) Test section core assembly with insulation.

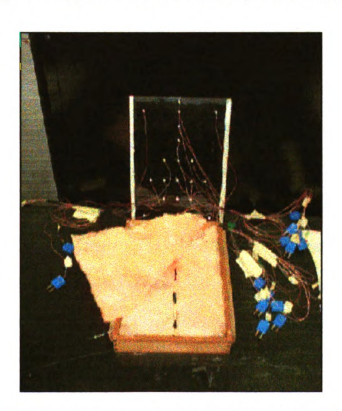


Figure 3.6. (b) Test section core assembly with thermocouples attached on the back surface of the test section and inside the insulation.

The second technique used a glass substrate coated with ITO film. The glass substrate was 1.1 ± 0.1 mm thick and the nominal ITO film thickness was 190A and had a resistivity of 75 ± 4.5 ohms per square area over its entire surface. The latter test section was selected because of its ease of use and flatness, which was desirable to avoid any disturbances to the hydrodynamic boundary layer. The former technique would be more useful for test sections with non-uniform shapes.

Electrical power was applied to the test section via thin stainless steel strips attached to the ITO film using Dynaloy 340 silver conductive paint [Dynaloy, Inc]. The silver paint had a resistivity of 0.001 ohms per 25m³. The paint was diluted using acetone and applied using a fine paint brush. The stainless steel strips were then laid on top. Applying pressure on the shim stocks using a Q-tip insured good contact. Two stainless steel strips were used, one along each edge of the test section (see Figure 3.7).

The two test sections were connected electrically in parallel to insure that both test sections received the same amount of power (see Figure 3.8). The power was supplied using a 6274B-HP DC power supply [Hewlett Packard Corp.]. The voltage and current were measured using a 177 Keithley digital multimeter [Keithley Instruments] at the end of each test. The resistance of the test section was temperature dependant, therefore, the voltage and current measurements were recorded after the test section reached a thermal steady state. Infrared and thermocouple measurements were acquired at that thermal steady state as will be discussed later. Representative voltage and current values were 50.7 ± 0.75 volts and 0.94 ± 0.026 amps, respectively. These values were chosen because

Figure 3.7. Test section and electrical connections.



Figure 3.8. Magnified view of the top surface of the test section core assembly.

they provided an average surface temperature of approximately 45°C, which was the surface temperature used for the isothermal boundary condition tests [Willenborg, 1996]. The test sections were painted with two layers of heat resistance and flat finish black paint [Chase Products Co.] to increase the surface emissivity for use with an infrared imaging camera to capture the surface temperature. The test sections were attached to the core using high temperature vacuum grease and were flush with the wall after insertion of the core assembly into the wall.

A total of 21 thermocouples were attached to the back surface of each test section (see Figure 3.6b). The purpose of these thermocouples was to provide data to compare with the IR measurements and to verify thermal symmetry on both sides of the wall. The thermocouples were attached to the glass surface using clear nail polish to establish good contact and quick adherence. Later, a high conductivity 200 Resin Omega Bound thermal paste [Omega Engineering, 1992] was applied on top of the interface between the thermocouple beads and the glass to strengthen the joint.

The measurements were taken after the test section reached a thermal steady state. The standard testing procedure was to turn on the wall jet air flow, turn on the power supply, and monitor the thermocouple measurements to determine when the test section reached a thermal steady state. This was determined when the difference between two consecutive measurements of each thermocouple was less than 0.1°C. Then the temperature from the IR camera and thermocouples, electrical voltage, and current measurements were obtained. The jet temperature was recorded using thermocouples that were inserted into

the plenum area.

3.2 Instrumentation

3.2.1 Infrared Imaging Camera

This study used an infrared thermal imaging camera to measure the surface temperature of the heated test section. All objects radiate heat as an electromagnetic wave. Common infrared detectors detect radiation in the 3-12 µm range. The IR camera used in this study was capable of detecting thermal radiation in the 8-12 µm range. Infrared thermal imaging was used because it is a non-intrusive measurement technique, it provides a comprehensive surface temperature measurements, and it is a rapid technique. The thermal imaging system used in this study was an Inframetrics 600L system (see Figure 3.9). The data acquisition and data analysis setup of the infrared thermal image is sketched in Figure 3.10.

The IR camera was capable of capturing data in both transient and steady state conditions. An average of 16 image fields for each data point was used in this study in an effort to reduce the noise in the infrared measurement. This IR camera averaging scheme decreased the measurement noise by a factor of four. The IR camera recorded the temperatures as gray level intensities and then the gray level intensities were converted to absolute temperatures using a pre-established linear relationship (see Appendix B). In this study, the data were recorded from the IR camera on a video tape as gray level intensities, then the image was captured using an image analysis software called Image Pro PlusTM [Media Cybernetics] and converted manually to absolute temperatures. Figure 3.10b shows a

schematic of the setup used to capture the thermal image. All test data were time marked using a VTG-33 timer [FOR.A Company Limited]. The data acquisition and image capturing setup included a TM-63U JVC monitor [JVC] and a AG-2400 Panasonic video cassette recorder[Panasonic].



Figure 3.9. The infrared imaging camera and system used to acquire data.

Calibration curves were established to convert the gray scale intensities recorded by the infrared camera to absolute temperatures using an area of view mode for the IR camera. The curves were established for the 10°C, 20°C, and 50°C temperature ranges. The calibration setup was similar to that used in Figure 3.10a. Electrical power was applied to a test specimen, which was constructed using a Kapton flexible space heater [Omega

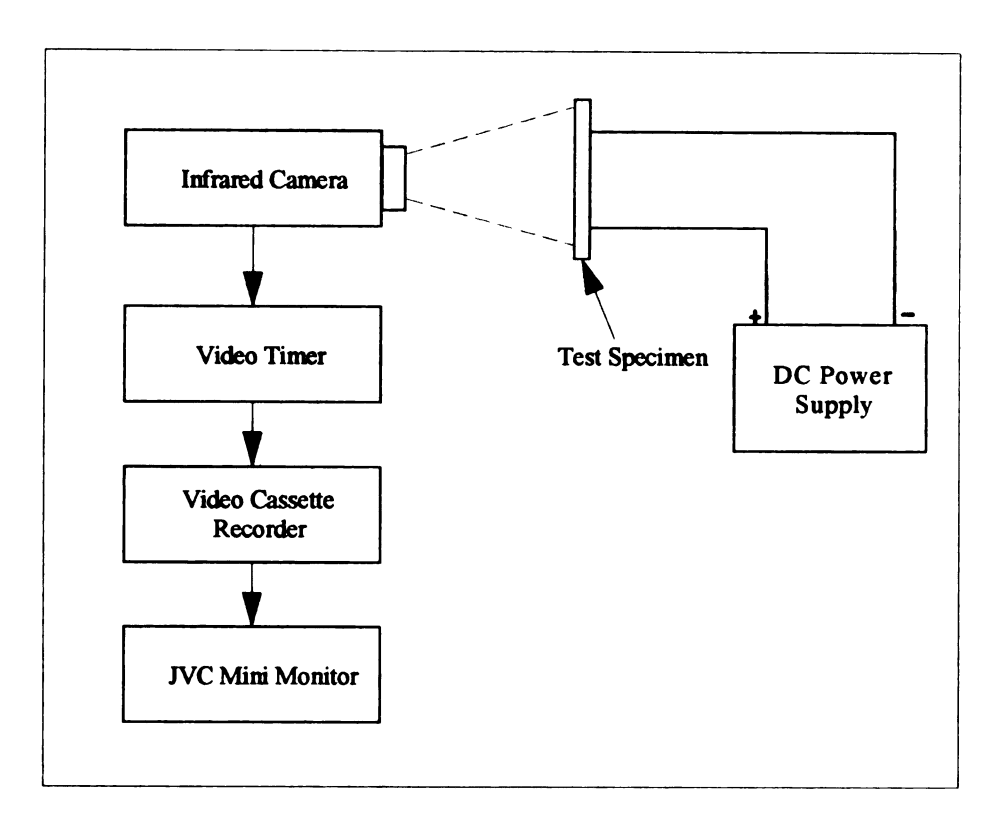


Figure 3.10. (a) Schematic of the setup used to acquire the infrared thermal image.

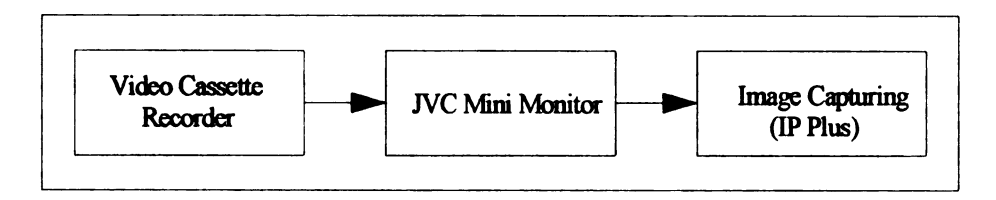


Figure 3.10 (b) Schematic of the setup used to capture the infrared thermal image for analysis.

Engineering, 92]. A 1.58 mm thick aluminum plate with the same surface area as the heater was mounted on each side of the heater and painted with black paint [Chase Products Co.]. The power was varied to produce several temperature levels as shown in Figures B1-B3, Appendix B. The data were acquired using the IR camera after the test section reached a thermal steady state. The minimum and maximum temperatures for each

test were recorded manually to establish the calibration equation. Further examination of the curves showed that the curves did not extend over the full range of the gray scale level. This decreased the IR camera resolution. These calibration curves included any bias error in the entire system, i.e. monitor, VCR, timer, and image board. Also, inherent in these calibration curves is the emissivity value of the black paint used in this study. The brightness and contrast levels of the image capturing software were manipulated to provide the largest possible range of gray scale to increase the resolution of the infrared measurements.

The emissivity of the black paint was determined to be 0.92 through preliminary calibration experiments. The setup of these preliminary experiments was similar to the schematic in Figure 3.10a. The emissivity calibration tests were conducted using two different specimens. One was constructed using the same material as the test specimen and the other using the Kapton flexible space heater [Omega Engineering, 92]. Black paint [Chase Products Co.] was applied to the surfaces of both specimens being imaged by the IR camera. A thermocouple was attached on the same surface. The emissivity value of the IR camera was adjusted using the control options until the IR camera temperature reading matched that of the thermocouple. The thermocouple was calibrated in boiling and freezing temperatures as will be described below. These tests were performed at room temperature and without flow. The test specimens were placed approximately 50 cm from the IR camera.

3.2.2 Thermocouples

Thermocouples were attached on the back surface of the test specimen. The labels and locations of these thermocouples are shown in Figure B.5. The thermocouples served two purposes. First, they provided data to verify the symmetry of the thermal boundary condition on both sides of the wall. Second, they were used to validate the measurements of the IR camera. Figure B.5a shows a frontal view of the thermocouples attached to the test section. Figure B.5b shows a side view of the thermocouples mounted inside the thermal insulation.

Engineering, 1992]. Calibration of the thermocouples were conducted at boiling and freezing temperatures. The boiling condition was simulated by boiling deionized water in a beaker over a space heater. Then the thermocouples were inserted individually into the beaker and the voltage produced were recorded. The freezing condition was produced by pouring cold deionized water into an insulated container filled with crushed ice and creating a slush ice bath. All the calibration data are presented in Table B1, Appendix B. All measurement deviations from the calibration point were within the reported manufacturer uncertainty which was the higher of 1.0°C or 0.75% of measurement above 0°C [Omega Engineering, 1992]. The readings of the thermocouples were recorded using an Omega hand held thermometer and calibrator unit model CL24 with a 0.1°C resolution and 0.1% of reading accuracy [Omega Engineering, 1992].

The thermocouple data were acquired using a Keithley Metrabyte DASTC data acquisition board [Keithley Instruments] during the wall jet experiment. The thermocouple sampling frequency was 3 samples/min, which was sufficient to capture steady state temperature data. The resolution of the board was 0.04°C [Keithley Instruments]. The accuracy of the A/D board was verified using a CL24 Omega calibrator unit as the temperature source. Up to 16 channels were used to acquire data simultaneously.

3.3 Uncertainty Analysis

The uncertainty of the local heat transfer coefficient was determined using the propagation of error technique. The technique is based on computing the error associated with each measured variable and determining its contribution to the final uncertainty value [Beckwith et al., 1993, Moffat, 1988, Kline and McClintock, 1953, and ANSI/ASME Measurement Uncertainty, 1985]. The error was computed using the following relationship:

$$\sigma_{x(i)}^{2} = \sum_{i=1}^{i=N} \left(\frac{\partial x}{\partial i} \Delta i \right)^{2}$$
 (3.1)

where i is equal to the number of independent variables used to calculate the quantity x, $\partial x/\partial i$ is the partial derivative of the quantity x to each independent variable, and Δi is the uncertainty of each independent variable. The uncertainty of h_x was computed by rewriting Eq. 2.1 in the following form:

$$h = \frac{q_{\text{total}} - q_{\text{cond}}}{(T_{s} - T_{j})A}$$
 (3.2)

and expanding Eq. 3.2 according to Eq. 3.1:

$$\Delta h = \left[\left(\frac{\partial h}{\partial q_{\text{total}}} \Delta q_{\text{total}} \right)^2 + \left(\frac{\partial h}{\partial q_{\text{cond}}} \Delta q_{\text{cond}} \right)^2 + \left(\frac{\partial h}{\partial T_s} \Delta T_s \right)^2 + \left(\frac{\partial h}{\partial T_j} \Delta T_j \right)^2 + \left(\frac{\partial h}{\partial A} \Delta A \right)^2 \right]^{\frac{1}{2}}$$
(3.3)

Equation 3.3 can be rearranged in the following form:

$$\Delta h = \frac{\left(q_{total} - q_{cond}\right)}{\left(T_{s} - T_{j}\right)A} \left[\left(\frac{\Delta q_{total}}{q_{total} - q_{cond}}\right)^{2} + \left(\frac{\Delta q_{cond}}{q_{total} - q_{cond}}\right)^{2} + \left(\frac{\Delta T_{s}}{\left(T_{s} - T_{j}\right)}\right)^{2} + \left(\frac{\Delta T_{j}}{\left(T_{s} - T_{j}\right)}\right)^{2} + \left(\frac{\Delta A}{A}\right)^{2} \right]^{\frac{1}{2}}$$

$$(3.4)$$

The form of Eq. 3.4 shows the effect of the individual quantities on the uncertainty of h_x. All terms in Eq. 3.4 are presented in Table 3.1. The method used to compute the uncertainty associated with each of the measured quantities is shown in Appendix C.

Table 3.1. Uncertainty terms used to compute the total uncertainty in h_x measurement.

Term Symbol	Uncertainty Value	
$\Delta q_{total}/(q_{total} - q_{cond})$	1.08E-03	
$\Delta q_{cond}/(q_{total} - q_{cond})$	1.46E-03	
$\Delta T_{s TC}/(T_{s TC} - T_i)$	5.38E-04	
$\Delta T_{sIR}/(T_{sIR} - T_i)$	1.89E-04	
$\Delta T_{jet}/(T_s - T_j)$	5.38E-04	
ΔΑ/Α	4.65E-05	
Δh_{TC} , W/(m ² K)	2.52E+00	
Δh_{IR} , W/(m ² K)	2.51E+00	

The largest contributor to the h_x estimated uncertainty is the conduction heat loss term followed by the total energy term. Detailed examination of the calculations, shown in Appendix C, revealed that the uncertainty in using thermocouple measurements to

determine the heat conduction losses were driving the conduction loss term to be the dominant source of measurement uncertainty. The electrical voltage term was causing the total energy term to be relatively high. Therefore, even though the temperature uncertainty did not appear to be a major contributor to the error uncertainty at first glance, detailed examination revealed that the temperature measurement uncertainty was the major contributor to the error uncertainty as shown in Appendix C.

In addition, an experimental uncertainty for h_x was calculated to be 8.3% using the standard deviation of a small population technique for 3σ [Beckwith et al.]. This means that the probability of Δh_x falling outside this experimental uncertainty is less than 0.3%. Table 3.2 summarizes both experimental and theoretical uncertainty values.

Table 3.2. Estimated and measured percent uncertainties of the local convection heat transfer coefficient.

Term	Percent Uncertainty	
Estimated Δh _{TC}	12.1 %	
Estimated Δh _{IR}	11.5 %	
Experimental Δh _{IR}	8.3 %	

The results in Table 3.2 indicate that the estimated uncertainty calculations were conservative and this experimental setup was a good approach in obtaining the local convection heat transfer coefficient measurements with low uncertainty error.

CHAPTER 4

RESULTS AND DISCUSSION

4.1 Velocity Profiles

All the measurements presented here were performed using an exit Reynolds number, Re_e , of 7.7×10^3 . This corresponded to an inviscid core exit velocity of 10 m/s or an area-averaged exit velocity of 6.1 m/s. The 6.1 m/s average velocity reflected the velocity magnitude in an actual automobile defroster. The non-dimensional velocity profiles are presented in Figure 4.1 [Willenborg, 1996]. These profiles were normalized in a similar fashion to the data reported in other investigations [Launder and Rodi, 1981]. Details of the measurement techniques used to obtain the velocity profiles were reported by Willenborg [Willenborg, 1996]. Three observations were made from the velocity measurements. First, a self-preservation form of the jet was established for x/w > 6.9 as shown in Figure 4.1b. Second, the curved streamlines in the developing region of the jet are an affect of the nozzle geometry, for $x/w \le 1.7$, which indicates the presence of a vena

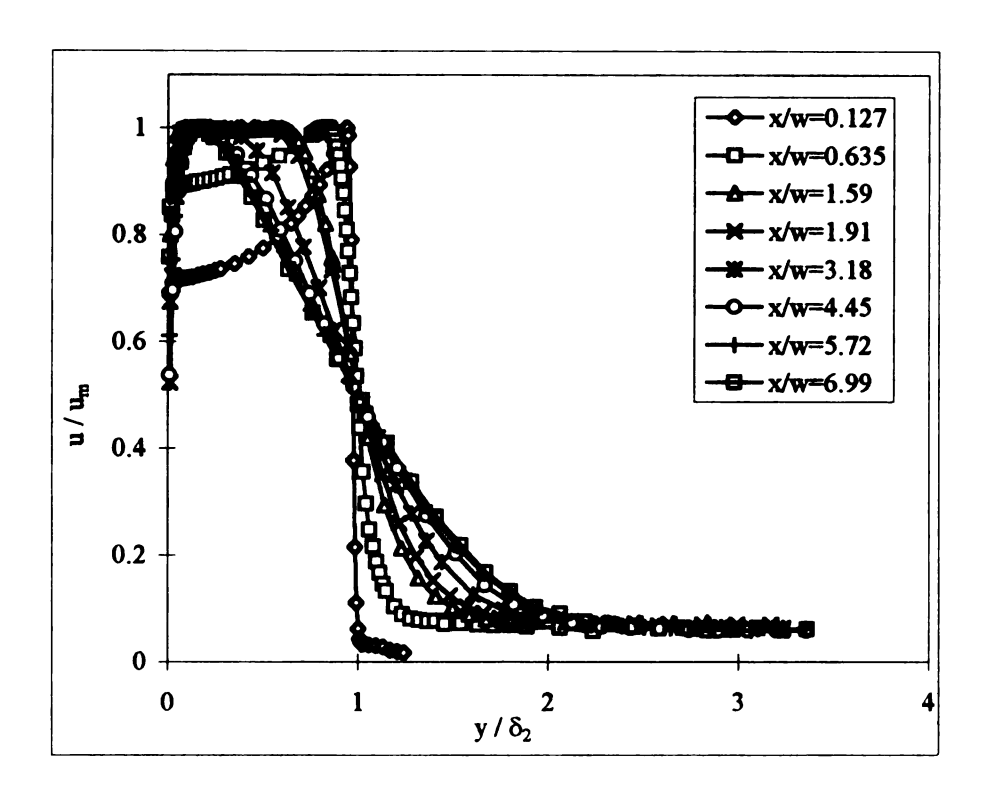


Figure 4.1. (a) Mean velocity profiles in developing region [Willenborg, 1996].

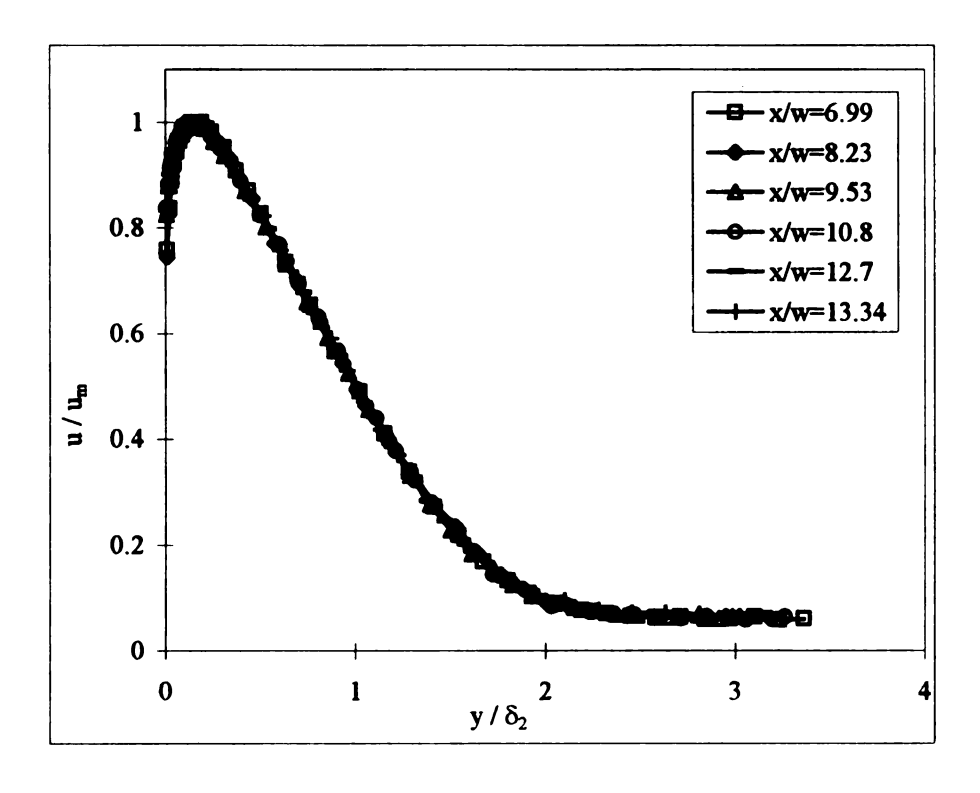


Figure 4.1 (b) Mean velocity profiles in self-preserved region [Willenborg, 1996].

contracta at that location as shown in Fig 4.1a. Third, the maximum velocity becomes less than the inviscid core velocity at $x/w \ge 4.4$, which may indicates the propagation of the outer shear effects into the inner boundary layer.

In order to compare to the data available in the literature, appropriate definitions of x_{ref} and w_{ref} were needed. The choices for x_{ref} and w_{ref} are dependent on the nozzle geometry and may vary from one study to another. It was determined that x_{ref} should start at the vena contracta and w_{ref} should be the width of the vena contracta for this study. At this location the velocity profile is similar to the velocity profile at the nozzle exits previously reported in the literature. The literature uses x_{ref} as the distance from the nozzle exit and w_{ref} as the nozzle width. Figure 4.1a supports the choice of x_{ref} and w_{ref} for this study because it demonstrates how the effect of the nozzle geometry on the velocity field dissipates at approximately $x/w \approx 1.7$, which is approximately the location of the vena contracta.

The growth of the hydrodynamic boundary layer was presented using the non-dimensional term δ_2/w_{ref} plotted against x_{ref}/w_{ref} as shown in Figure 4.2. The slope of the line representing the growth of the boundary layer was 0.073 for $x_{ref}/w_{ref} > 6.9$ where self-preservation was reached. This is in agreement with the reported value of 0.073 [Launder and Rodi, 1981].

Another method of validating the wall jet profile used in the present study was to compare the decay of the maximum wall jet velocity. Sigalla reported this decay for $x_{ref}/w_{ref} \ge 20$ in

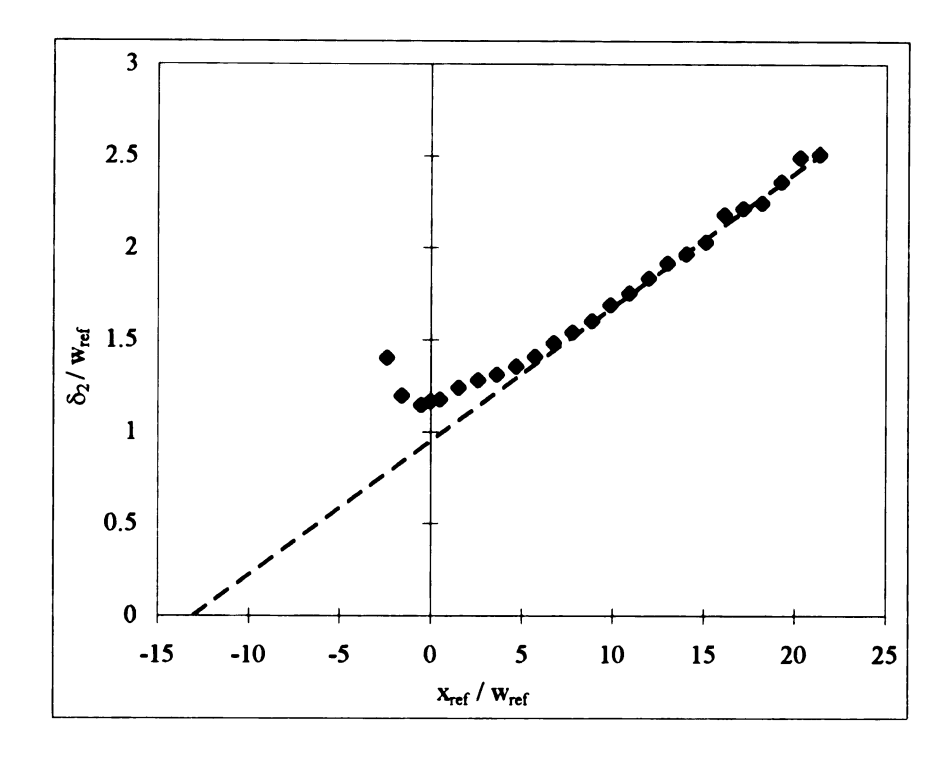


Figure 4.2. Development of the characteristic jet width, δ_2 [Willenborg, 1996].

the following form:

$$\frac{u_{m}}{u_{ref}}\sqrt{\frac{x_{ref}}{w_{ref}}} = 3.45 \tag{4.1}$$

Figure 4.3 shows the maximum velocity decay function in the same form as Eq. 4.1. The decay function of the data presented here was still rising and approaching that reported by Sigalla in Eq. 4.1. The results presented by Sigalla were for a fully developed turbulent wall jet, while the results presented in this study were for a developing wall jet. Therefore, it was expected that the two decay functions will have the same constant values at larger x_{red}/w_{ref} values.

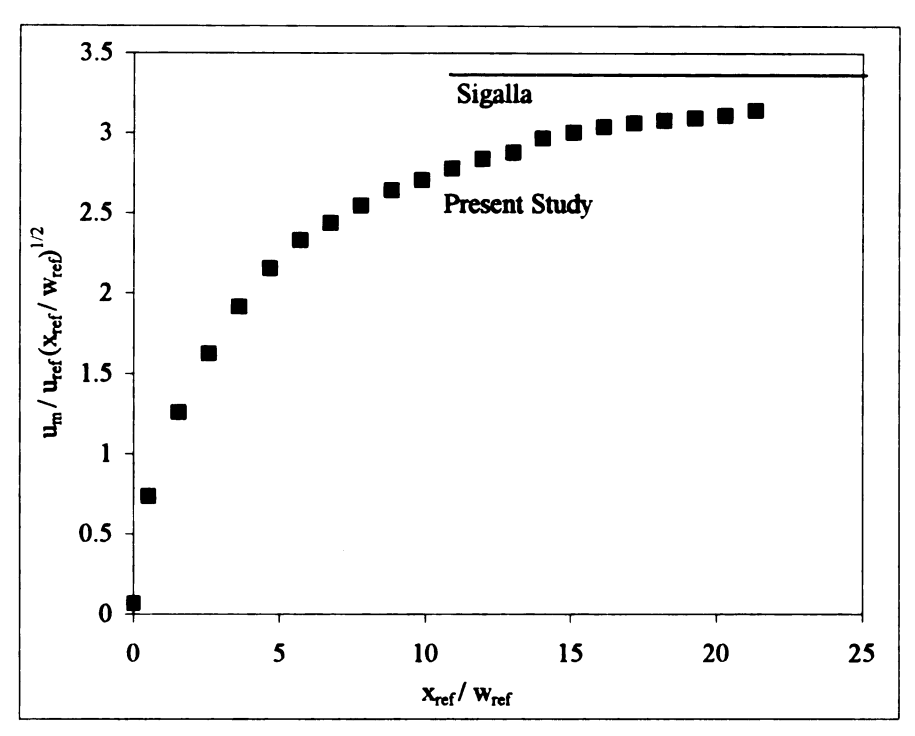


Figure 4.3. Maximum velocity decay behavior [Willenborg, 1996].

4.2 Uniform Heat Flux Boundary Condition

4.2.1 Temperature Profiles

Figure 4.4 shows a representative 3-D infrared thermal image of the test section temperature distribution obtained using the IR camera. The average air jet velocity, u_{vc}, was 10 m/s at the vena contracta and the total convection heat flux was 1023 W/m². A 2-D temperature profile of Figure 4.4 is shown in Figure 4.5. The surface temperature distributions were very reproducible as can be seen in Figure D1-D4, Appendix D. Careful examination of Figures 4.4 and 4.5 reveals that the temperature field was adequately symmetric. Infrared imaging data show some non-symmetry in the area of higher temperature profile or lower heat transfer. However, thermocouple data on each side of the centerline of the test section were similar to each other and within the thermocouple

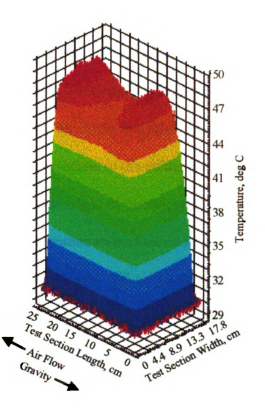


Figure 4.4. 3-D infrared surface temperature contour with $q^{\prime\prime}_{\rm conv}=1023~W/m^2$ and $u_{ref}=10~m/s.$

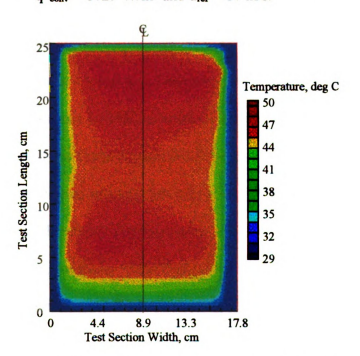


Figure 4.5. 2-D infrared surface temperature profile with $q^{\text{"}}_{\text{conv}}=1023~\text{W/m}^2$ and $u_{\text{ref}}=10~\text{m/s}$.

measurement uncertainty. Another important observation was the reduction of the temperature toward the trailing edge of the test section. It is believed that this was a result of the change in thermal boundary condition upstream of the trailing edge of the test section. This change in thermal boundary condition resulted in conduction heat losses from the trailing edge of the hot test section to the colder surrounding wooden wall. These effects were also seen at the side edges of the test section (see Figure 4.5). The same behavior was seen in all the experiments performed in this study. This kind of behavior was not reported in the literature and it will not be considered in the discussion of results that will follow because it did not affect the fluid mechanics or heat transfer characteristics of the wall jet in the region where this research was focused.

Figure 4.6 shows a representative temperature profile along the centerline of the test section using the IR camera and thermocouples attached on the backside of the front test section. The IR measurement line was coincident with the line of the thermocouples. The temperature profile from Figure 4.6 was non-dimensionalized according to Eq. 2.15 and plotted in Figure 4.7. This scheme was chosen because it used the line-averaged surface temperature of both infrared and thermocouple measurements to eliminate any bias difference effects between the two measurement techniques. These bias errors were inherent in the infrared and thermocouple measurements such as the uncertainty of the gray scale calibration curves, emissivity of the black paint, distance from the IR camera to the test section, and the uncertainty of the A/D board used to capture the thermocouple measurements

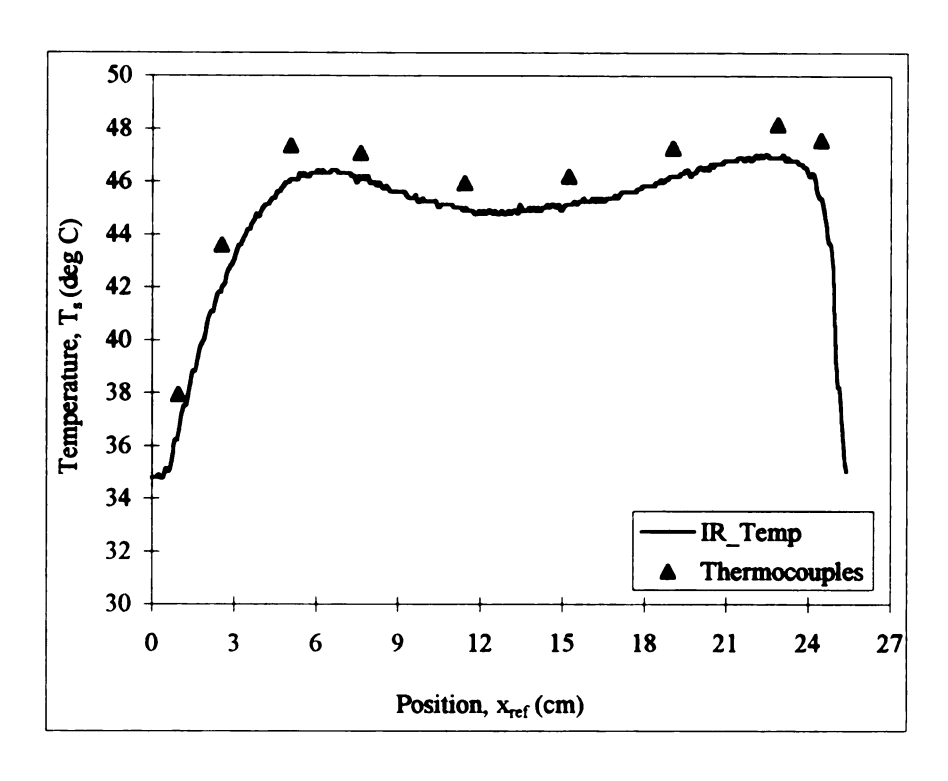


Figure 4.6. Temperature as a function of position using infrared camera and thermocouple data.

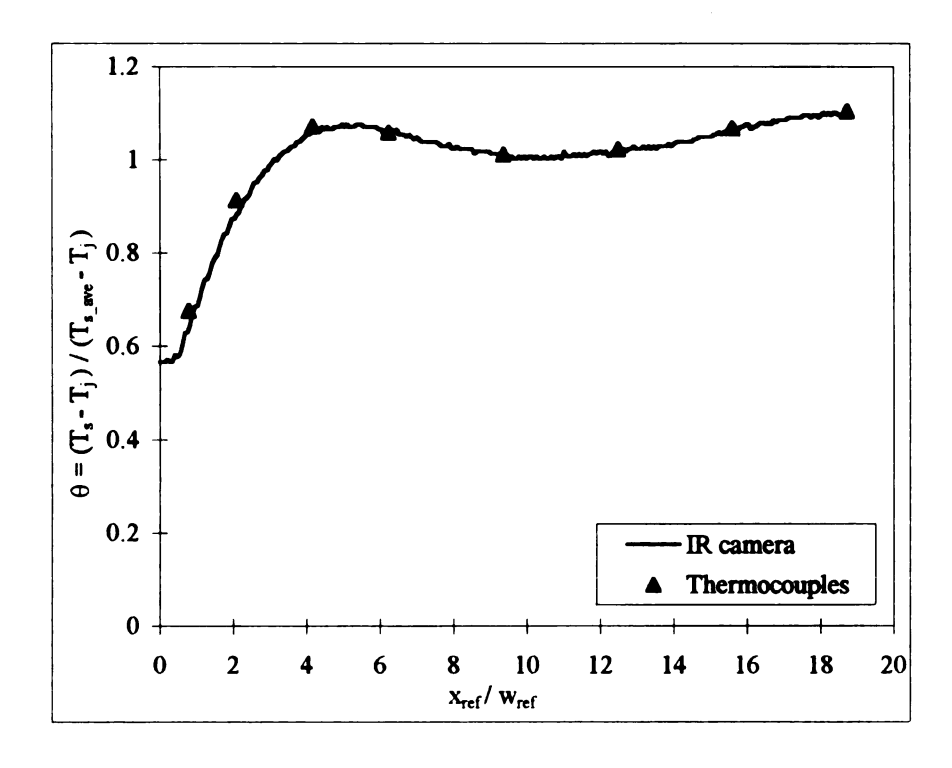


Figure 4.7. Non-dimensional temperature profile along the centerline of the heated test section for the isoflux case.

The temperature data using the IR camera were always approximately 2-2.5% lower than the data using the thermocouples. Physically this could not be true because the heat flux was being applied to the front surface of the test section where the IR camera was imaging while the thermocouples were attached on the back surface. This phenomenon was seen in all experiments conducted in this study. This difference was within the IR camera and thermocouple measurement uncertainty and could be explained by the bias error inherent in both measurement techniques as discussed previously.

The symmetry of the hydrodynamic and thermal boundary conditions was monitored using thermocouples attached on both front and back test sections (see Figure B.5a). Figure 4.8 shows thermocouple measurements corresponding to the same location on the front and

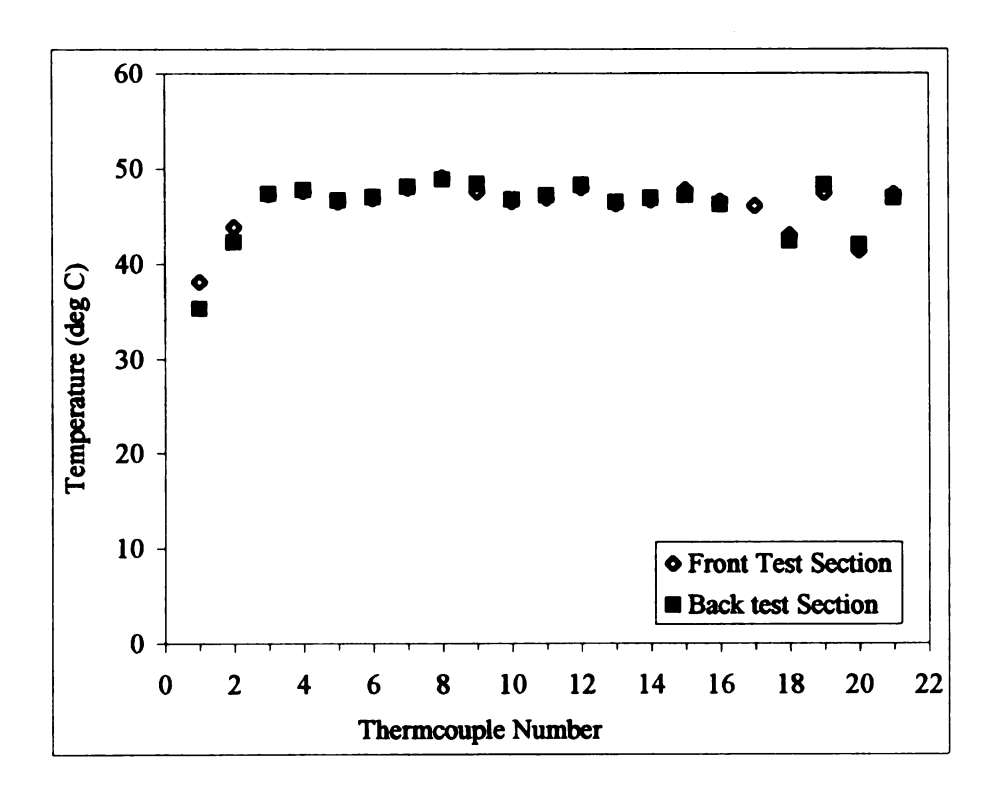


Figure 4.8. Thermocouple data of the front and back test sections.

back test sections. The difference in the measurements was negligible with respect to the estimated thermocouple measurement uncertainty. Therefore, symmetry was achieved between the two sides of the wall.

The temperature warm up history in the test section and the insulation is shown in Figures 4.9 and 4.10. Thermocouples 50 through 55 were mounted inside the insulation as shown in Figure B.5b. Figure 4.11 shows the cool down profile of the test section and the insulation. The x and y values in Figures 4.9-4.11 are indicative of the thermocouple locations on the test section or inside the insulation (see Figure B.5a and B.5b). It can be seen that the test section and the insulated core reached steady state after 15 minutes during warm up and after 25 minutes during cool down.

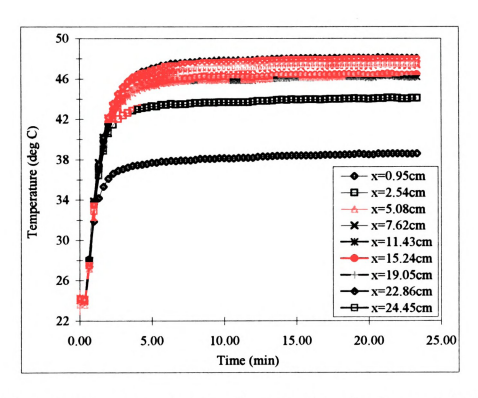


Figure 4.9. Temperature warm up history of the test section using thermocouple data.

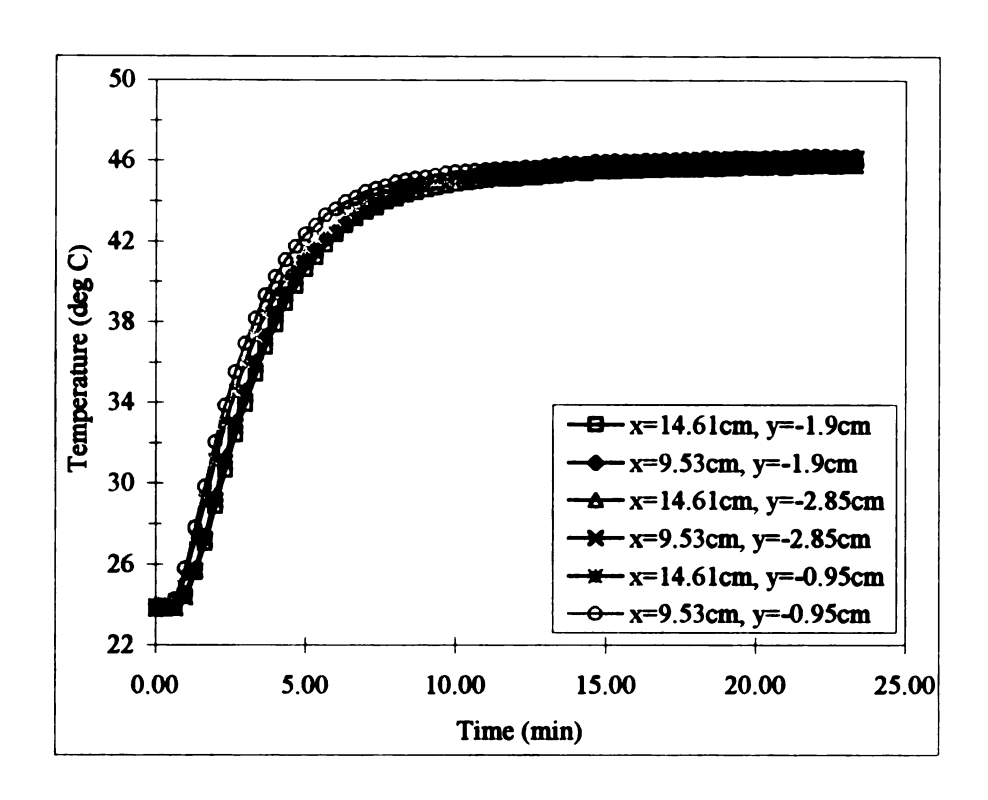


Figure 4.10. Temperature warm up history of the insulation using thermocouple data.

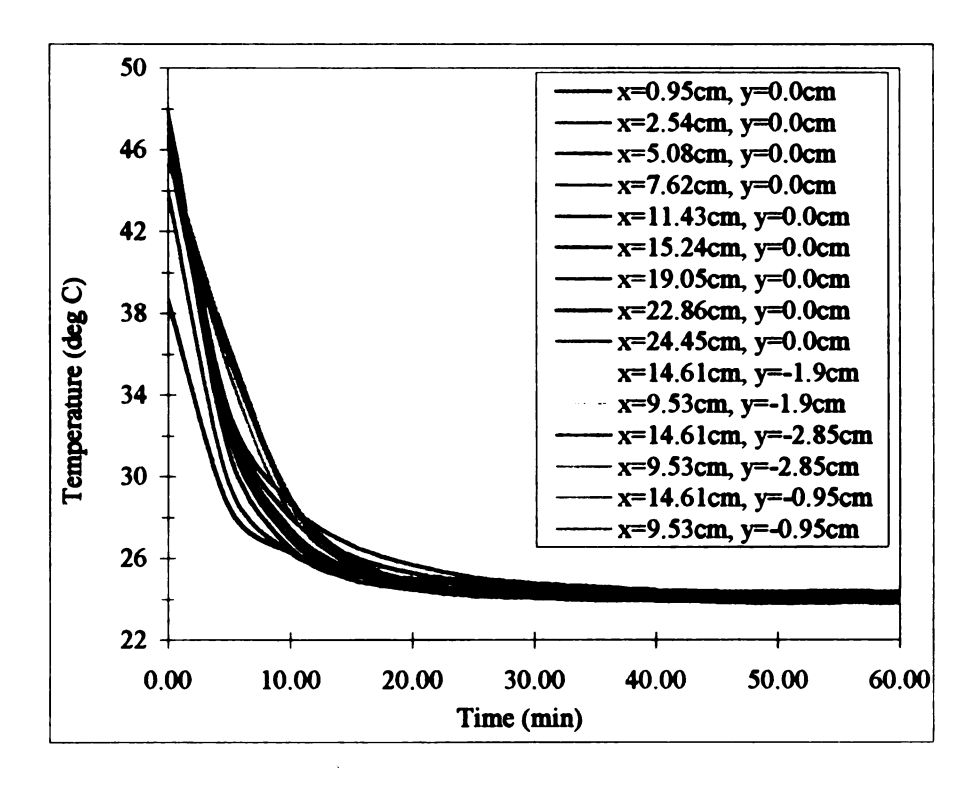


Figure 4.11. Temperature cool-down history in the test section and insulation using thermocouple data.

4.2.2 Local Convection Heat Transfer Coefficient

The local heat transfer coefficient is plotted in Figure 4.12 using the temperature measurement from Figure 4.6. Figure 4.13 shows the local heat transfer coefficient plotted against x_{ref}/w_{ref} for this study to allow a more direct comparison with available data in the literature. The following observations can be made from examining Figure 4.13:

- 1) The rapid decrease of h_x from the leading edge of the test section.
- 2) The decrease to a minimum h_x value at $x_{ref}/w_{ref} \approx 4$.
 - 3) The increase to a maximum h_x value at $x_{ref}/w_{ref} \approx 11.5$.
 - 4) The continuing decline of h_x as x_{ref}/w_{ref} increases.
 - 5) The difference between the infrared camera and thermocouples data was within the

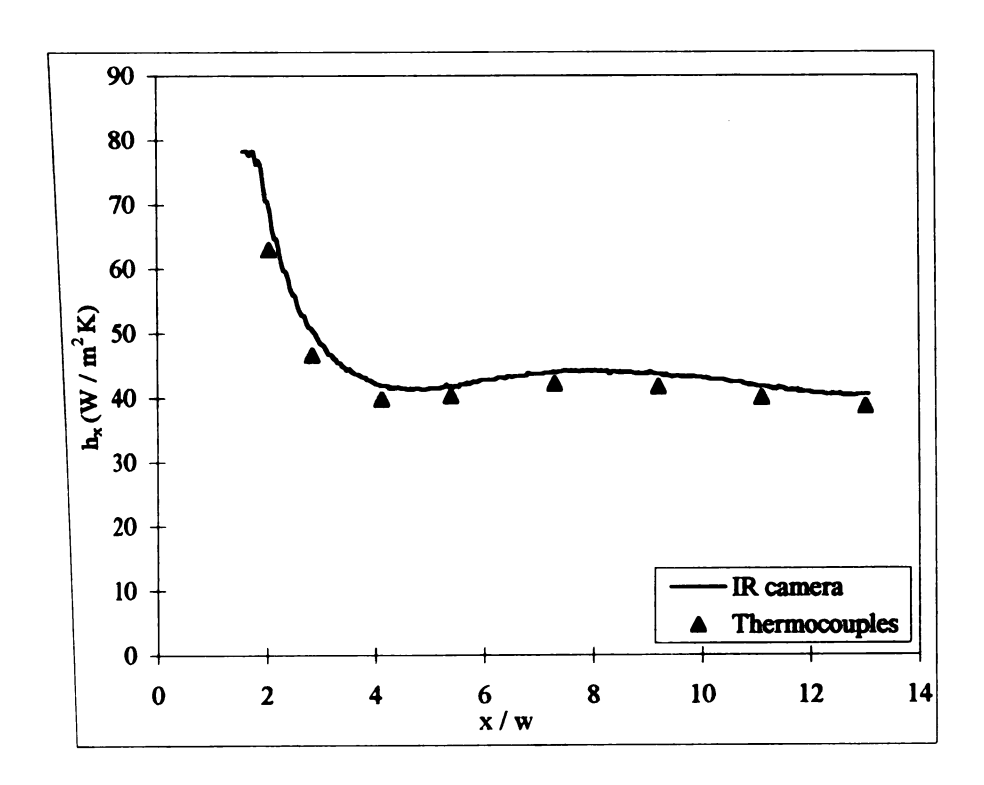


Figure 4.12. Local convection heat transfer coefficient for the isoflux boundary condition.

estimated uncertainty of both measurements as shown using the error uncertainty bars in Figure 4.13.

The increase in h_x for $4 \approx x_{ref}/w_{ref} \approx 11.5$ was thought to be a result of the outer shear layer propagating into the inner boundary layer. The subsequent decrease in h_x values for $x_{ref}/w_{ref} \ge 11.5$ was interpreted to be an effect of the thermal boundary layer growth.

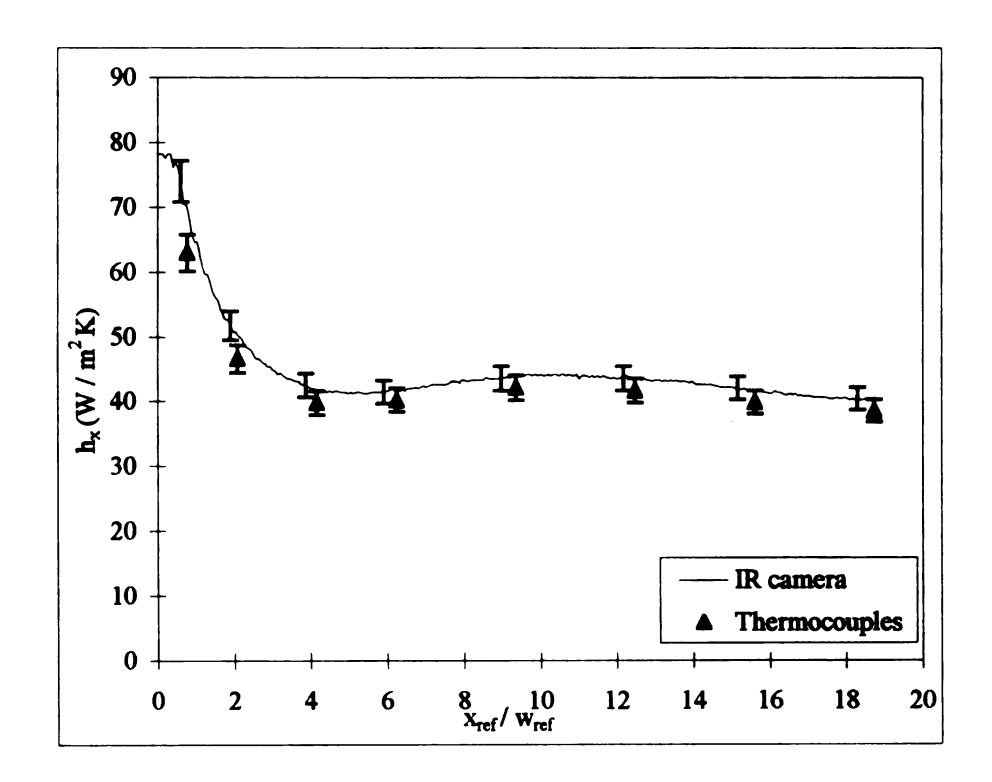


Figure 4.13. Local convection heat transfer coefficient as a function of x_{ref}/w_{ref} for the isoflux boundary condition.

4.2.3 Non-Dimensional Local Convection Heat Transfer Coefficient.

Figure 4.14 shows the non-dimensional heat transfer coefficient plotted against x_{ref}/w_{ref} using IR camera data. The non-dimensional heat transfer coefficient was calculated using Eq. 2.11.

The same behavior of the Nusselt number was seen by Akfirat in his heat transfer study [Akfirat, 1966] and by Mabuchi and Kumada in their mass transfer study [Mabuchi and Kumada, 1972]. Mabuchi and Kumada used mass transfer analogy to deduce Nusselt number values from Sherwood number measurements. The data presented in both references, as seen in Figure 4.15, showed a distinct minimum Nusselt number for the same order of magnitude of Re_e at $x_{ref}/w_{ref} \approx 4$ and a maximum Nu_{ref} at $x_{ref}/w_{ref} \approx 12$, where they defined x_{ref} and w_{ref} as the axial distance from the nozzle exit and the nozzle exit width, respectively. The data presented in this study showed a distinct minimum at $x_{ref}/w_{ref} \approx 4$ and maximum at $x_{ref}/w_{ref} \approx 11.5$.

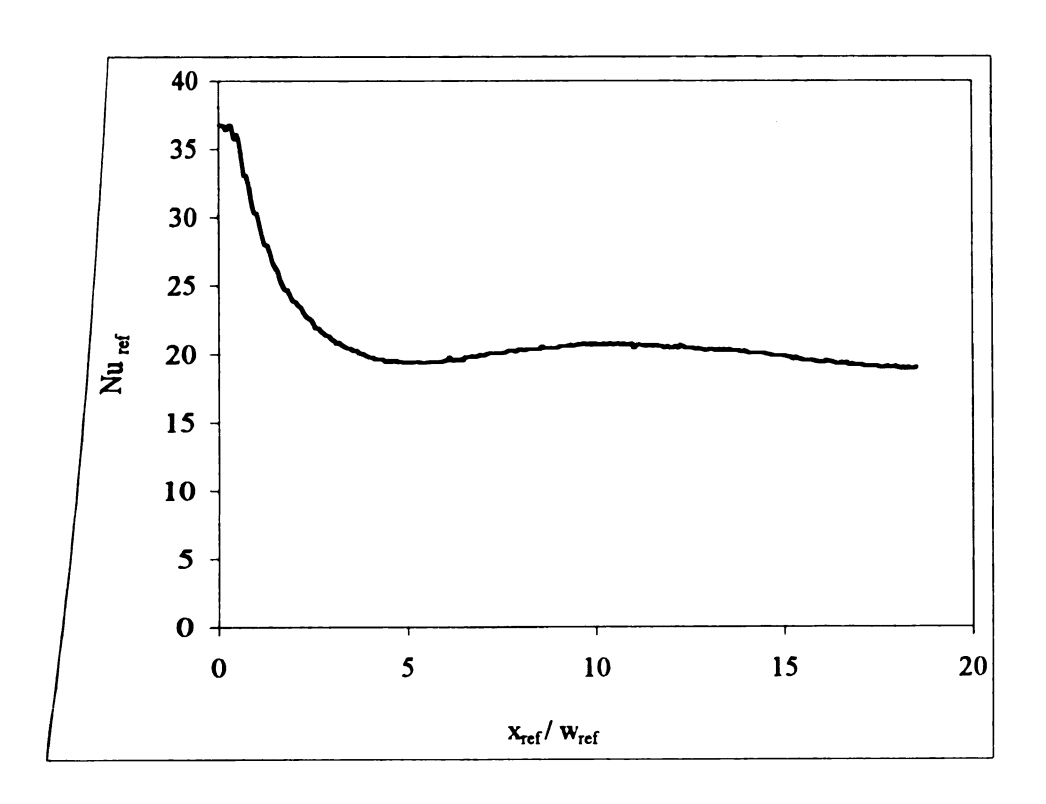


Figure 4.14. The non-dimensional local convection heat transfer coefficient using infrared camera data.

In an attempt to correlate the data presented here with other investigations, the maximum Nusselt number was computed. Mabuchi and Kumada used their data along with Akfirat's data of the maximum Nu_x to develop the following relationship [Mabuchi and Kumada, 1972]:

$$Nu_{ref,max} = 0.064 Re_{ref}^{2/3} Pr^{0.43}$$
 (4.2)

Nu_{ref,max} for this study was plotted as a function of the correlation in Eq. 4.2 and the results compared well. Figure 4.15 shows that the magnitude of the minimum Nu_x for the present study did not compare well with the published data. This is a result of the different nozzle geometry and exit velocity prfoile which have a large influence on the flow field at small x/w.

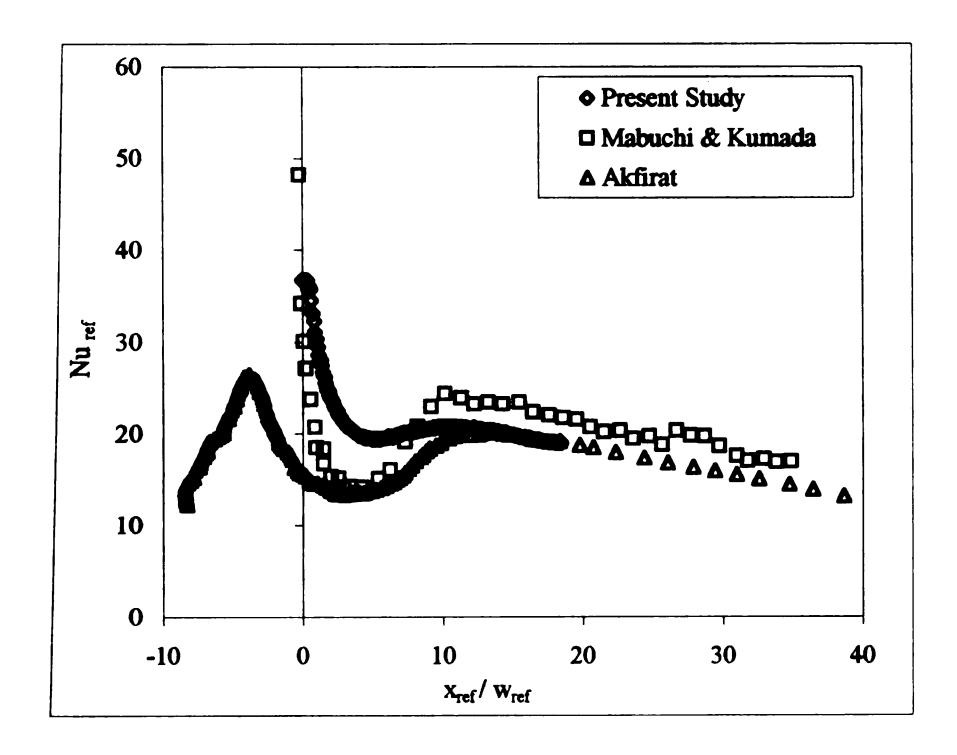


Figure 4.15. Comparison of the Local Minimum Non-dimensional Convection Heat Transfer Coefficient.

A comparison with published empirical correlations was performed by plotting the reference Nusselt number from the present study and from Akfirat and Mabuchi and Kumada in Figure 4.16. It is apparent that the Nu_{ref} from this study appears to approach the ones from the other studies if it is extended to larger x_{ref}/w_{ref} values. A direct comparison was not possible because the available heat transfer correlations were for a fully turbulent jet, where $x_{ref}/w_{ref} \ge 30$ and for different jet nozzle geometry.

Another comparison with published empirical correlations was performed using the correlation presented in Eq. 2.10. Again, a direct comparison between the data presented here and other investigations was not possible because the data presented here were for $x_{ref}/w_{ref} \le 20$ while the published correlations, in the form of Eq. 2.10, were for $x_{ref}/w_{ref} \ge 30$.

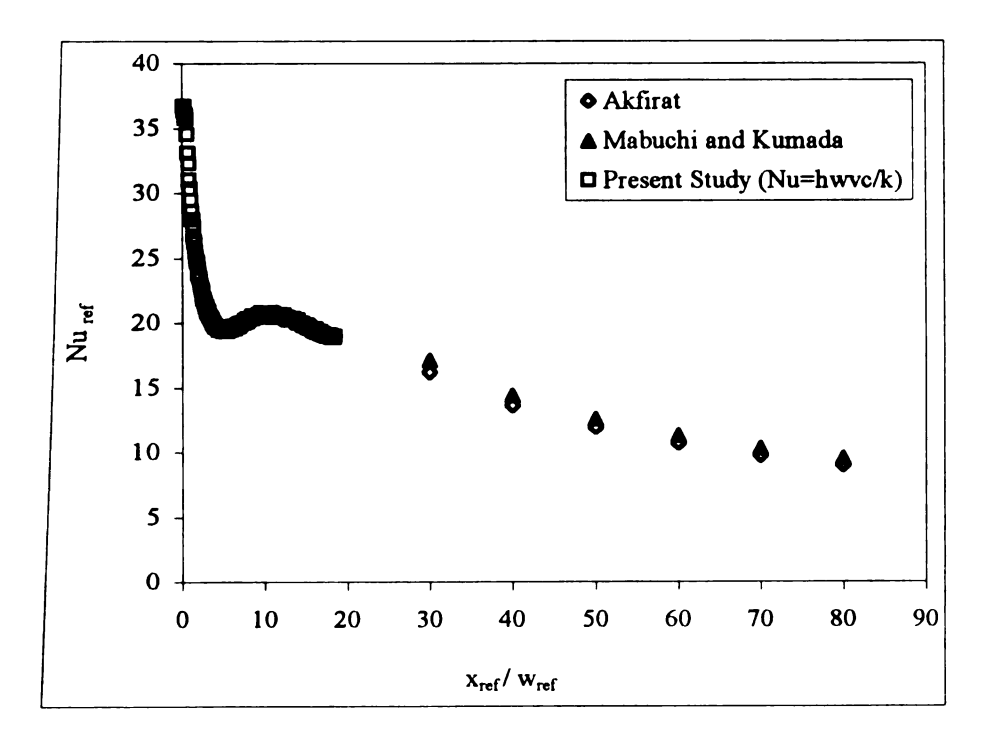


Figure 4.16. Comparison of present Nusselt number streamwise distribution with published data.

Figure 4.17 is a plot of the quantity Nu_{ref} (Re_{ref})^{-0.8} as a function of x_{ref}/w_{ref} for the data presented here and the correlations provided by Akfirat [Akfirat, 1966] and Mabuchi and Kumada [Mabuchi and Kumada, 1972]. These correlations were representative of the correlations reported by other investigators. It is apparent that the data presented here, if extended to $x_{ref}/w_{ref} \ge 30$ would approach those data presented by Akfirat and Mabuchi.

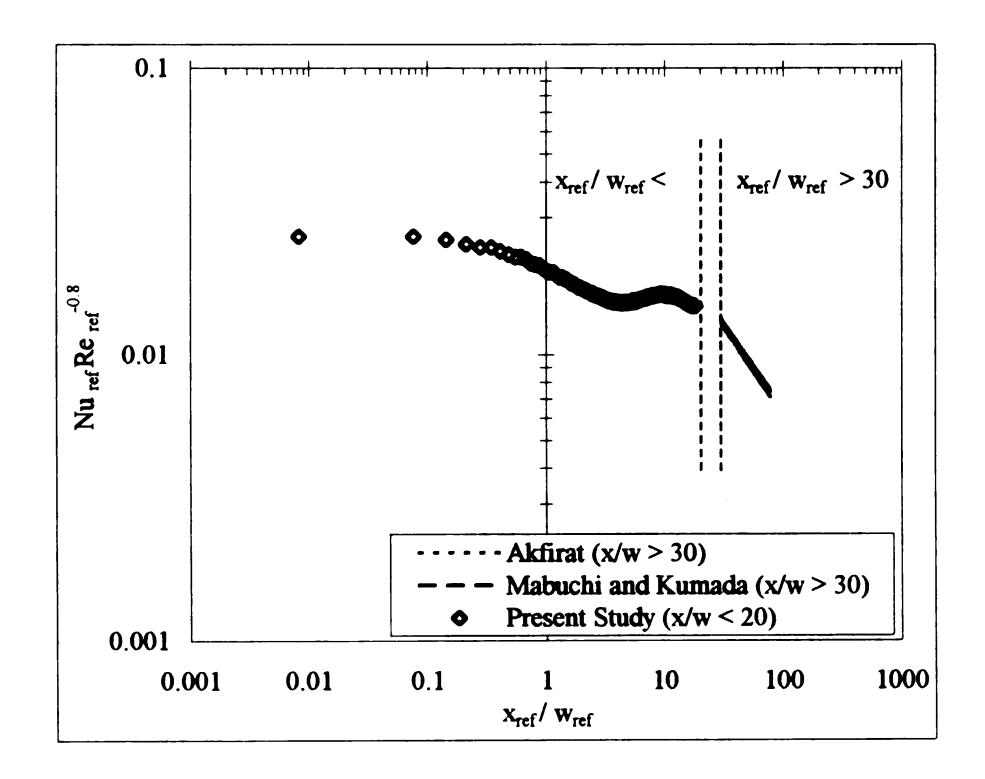


Figure 4.17. Comparison of the present Nusselt number with published empirical correlations.

4.3 Local Convection Heat Transfer Coefficient for Isoflux and Isothermal Boundary Conditions.

Figure 4.18 shows a comparison between h_x values for the isoflux and isothermal boundary conditions. Details of the isothermal measurements are provided by Willenborg [Willenborg, 1996]. Measurements of both boundary conditions were performed using the

same experimental configuration and parameters (average jet velocity, jet temperature, and nozzle width).

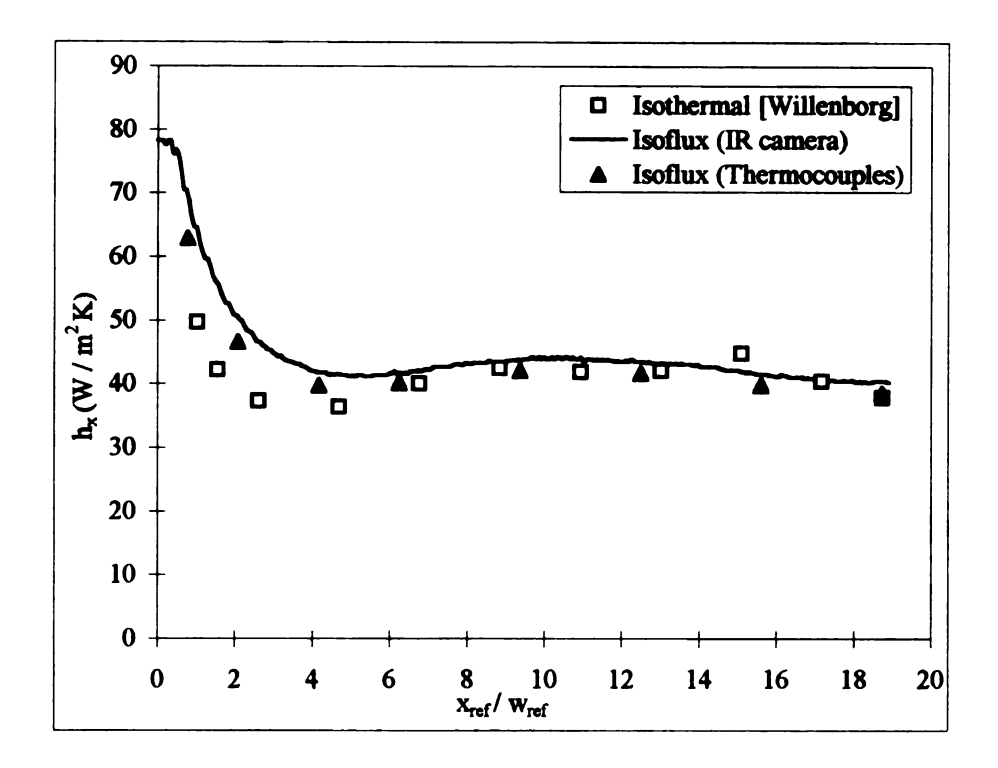


Figure 4.18. The local convection heat transfer coefficient for isoflux and isothermal boundary conditions.

The h_x values were approximately 30% higher for the isoflux case than the isothermal case near the leading edge of the test section (see Figure 4.19). This difference decreased to approximately 5% at $x_{ref}/w_{ref} \ge 5$. The difference was within the estimated error of both techniques. The large difference at the leading edge is an indication of a laminar flow. However, as the flow becomes more turbulent, the difference decreases. This behavior is similar to the heat transfer behavior for laminar and turbulent flows over a flat plate [Incropera and DeWitt, 1990].

1.4

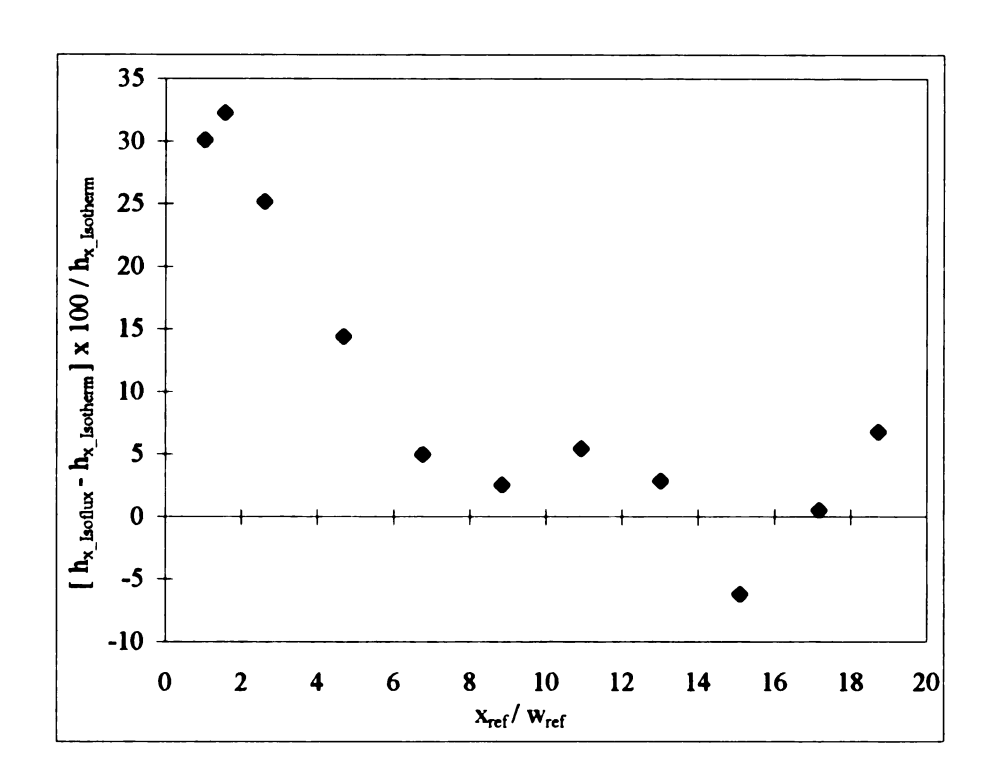


Figure 4.19. Percent variation of the local convection coefficient between the isothermal and isoflux boundary conditions.

CHAPTER 5

CONCLUSIONS AND RECOMMENDATIONS

5.1 Conclusion

An experimental system was developed and used to generate benchmark data for a model heated wall jet flow using conditions relevant to automotive defrosters. These data have permitted our sponsor, the Ford Motor Co., to evaluate the numerical simulations that are used to compute such flows. This experimental facility provides a two-dimensional wall jet with a heated wall that can be configured to present a uniform temperature or uniform heat flux boundary condition. This experimental configuration has the advantage of geometrical and thermal simplicity in comparison to actual defroster configurations.

Measurements of the local convection heat transfer coefficient for a uniform heat flux boundary condition were presented. Measurements were made for relatively small non-dimensional streamwise locations ($0 \le x_{ref}/w_{ref} \le 20$) suggested by the motivational problem: the defroster flow in an automotive vehicle. The non-dimensional streamwise

location was defined using the origin of the wall jet at the vena contracta. It was there that the wall jet velocity profile was similar to the profile generated by contour nozzles that were used by other investigators.

A local minimum heat transfer coefficient was observed at approximately $x_{ref}/w_{ref} \approx 4$ and a local maximum heat transfer coefficient was observed at $x_{ref}/w_{ref} \approx 11.5$. This agreed with available data for heat transfer coefficients for relatively small x_{ref}/w_{ref} . Direct comparison with previous results was not possible because most published data were for large x_{ref}/w_{ref} , different nozzle geometries, and different exit Reynolds numbers. However, extrapolation of the present results would appear to be consistent with previous results at larger streamwise locations.

The results suggest that the use of infrared imaging technology is an accurate and rapid method of determining the distribution of the local convection heat transfer coefficient for the isoflux boundary condition case. The estimated uncertainty for the h_x was less than the calculated experimental uncertainty using infrared measurements. The uncertainty analysis revealed that the energy loss term is the major contributor to the uncertainty associated with the h_x measurement.

Finally, the results showed that the local heat transfer coefficient was sensitive to the thermal boundary condition at small downstream locations and insensitive to the thermal boundary condition at sufficiently large downstream locations ($x_{ref}/w_{ref} \ge 5$) where the outer turbulent layer has diffused into the inner region of the wall jet. In this region, the

difference in h_x values between the isothermal and isoflux boundary conditions was within the estimated uncertainty of both measurement techniques.

5.2 Recommendations

Future studies should systematically introduce the complexities associated with the actual windshield defrosters. These complexities include 3-D flow, impinging flow, variation of non-heated starting length, and variation of the jet exit Reynolds number.

APPENDIX A

Conduction and Convection Heat Transfer Thermal Resistance Analysis This appendix will present the thermal resistance analysis performed when selecting the test section used in this study. It was important that the test section have relatively high resistance to conduction heat transfer in comparison to convection heat transfer. This insured that the energy supplied to the test section was dissipated to the wall jet via convection heat transfer and not dissipated through the test section through conduction heat transfer.

The glass test section was selected because of its low thermal conductance. The ratio of conduction to convection heat transfer thermal resistance was computed using:

$$\frac{R_{\text{cond}}}{R_{\text{conv}}} = \frac{\left(\frac{t}{k_{\text{glass}}A}\right)}{\left(\frac{1}{h_{\text{ave}}A}\right)}$$
(A.1)

where R_{cond} , and R_{conv} are the thermal resistance to conduction and convection heat transfer, respectively, t is the thickness of the test section, k_{glass} is the thermal conductivity of the glass test section, A is the test section surface area, and k_{ave} is the average convection heat transfer coefficient. Equation A.1 was reduced to:

$$\frac{R_{cond}}{R_{conv}} = \left(\frac{h_{sve}t}{k_{glass}}\right) \tag{A.2}$$

Eq. A.2 was evaluated using actual experimental values:

$$\frac{R_{cond}}{R_{conv}} = \left(\frac{43.5 (W/m^2 k) \times 1.1 \times 10^{-3} (m)}{1.4 (W/m k)}\right)$$
$$= 3.4 \times 10^2$$

This analysis shows that the thermal resistance to conduction heat transfer is two orders of magnitude higher than the resistance to convection heat transfer.

APPENDIX B

Calibration Curves and Data for Infrared Imaging and Thermocouple Measurement Techniques This appendix will present the calibration data for the infrared and thermocouple measurement techniques. The appendix will be divided into two sections. Section B.1 will present and discuss the calibration curves associated with the IR camera measurements. Section B.2 will present and discuss the calibration data associated with thermocouple measurements.

B.1 Calibration Curves for Infrared Measurements

The temperature was captured by the infrared camera as gray scale intensities. These gray scale values were converted to absolute temperatures using calibration curves as discussed in the experimental methodology chapter. Figures B.1-B.3 present the curves used in this study for the 10°C, 20°C, and 50°C temperature range, respectively.

A linear fit was used to generate the calibration equation. This equation was made universal using a non-dimensional temperature and the minimum and maximum surface temperature. Figure B.4 combines the results of the 10°C, 20°C, and 50°C temperature ranges in one calibration equation. This shows that one calibration equation may be sufficient for all temperature ranges used in this study.

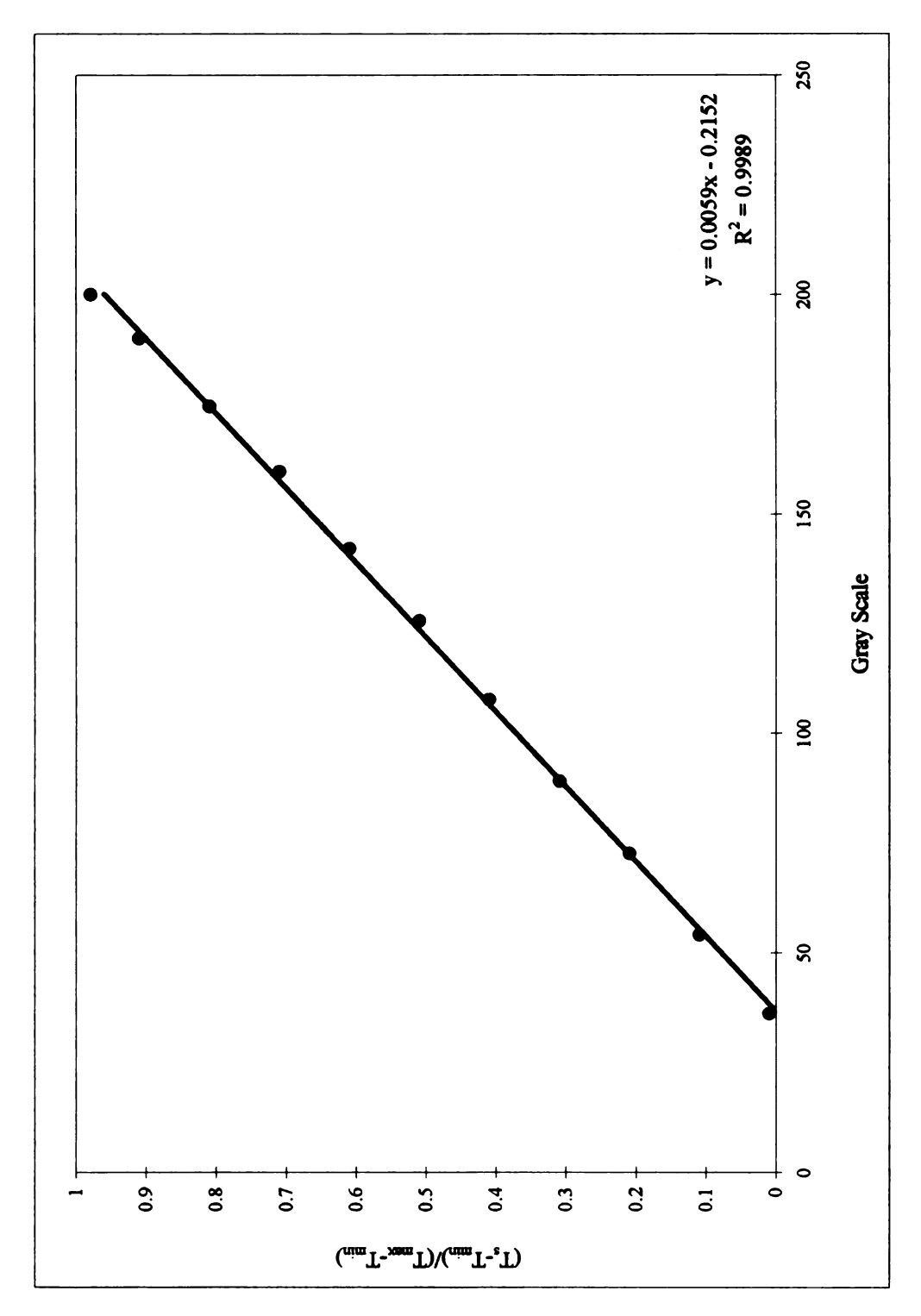


Figure B.1. Infrared camera calibration curve for the 10C temperature range. Other imaging parameters were: $T_{min} = 40C$, $T_{max} = 50C$, brightness level = 52 and contrast level = 72.

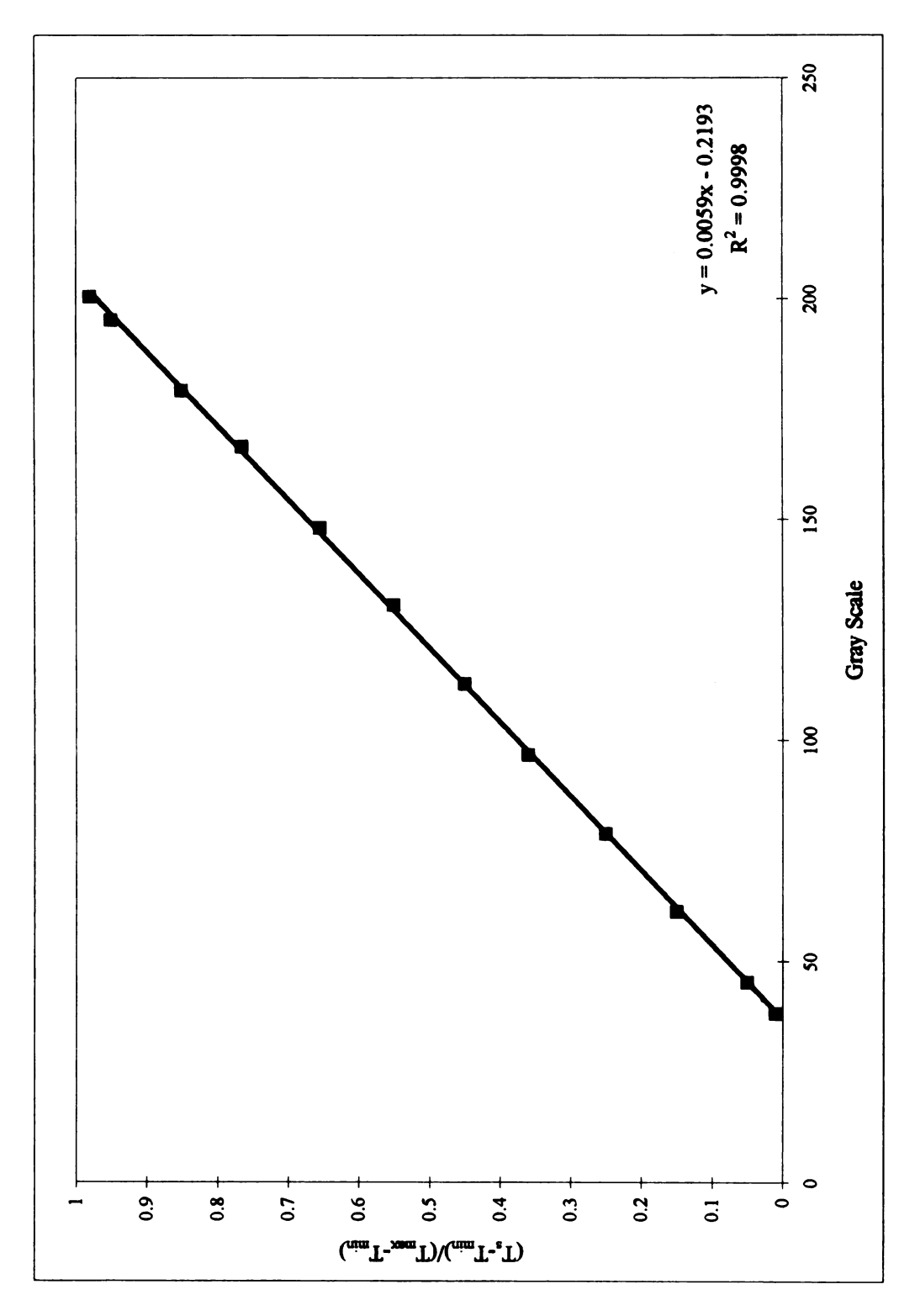


Figure B.2. Infrared camera calibration curve for the 20C temperature range. Other imaging parameters were: $T_{min} = 35.1C$, $T_{max} = 55.1C$, brightness level = 52 and contrast level = 72.

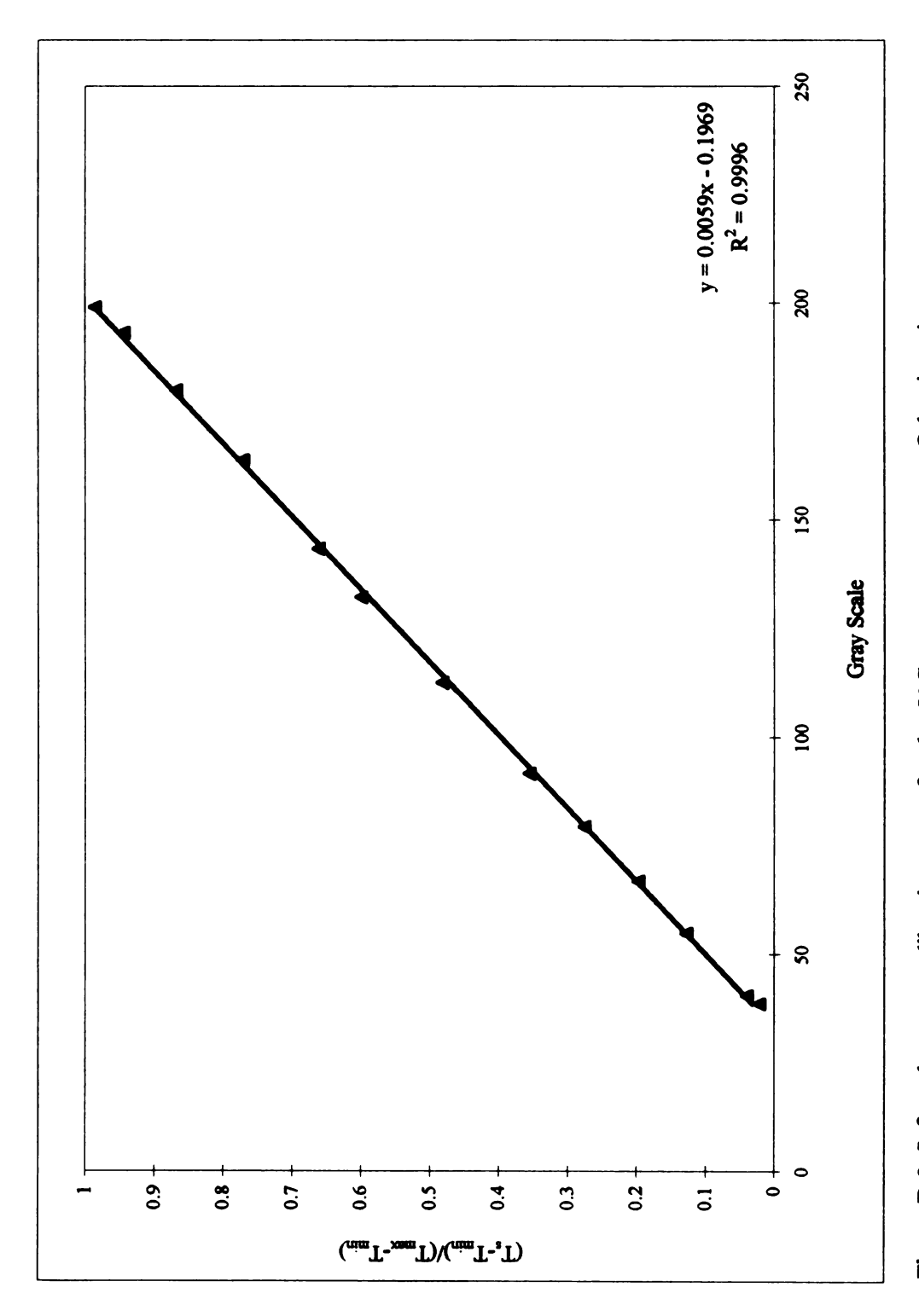


Figure B.3. Infrared camera calibration curve for the 50C temperature range. Other imaging parameters were: $T_{min} = 35.5C$, $T_{max} = 85.5C$, brightness level = 52 and contrast level = 72.

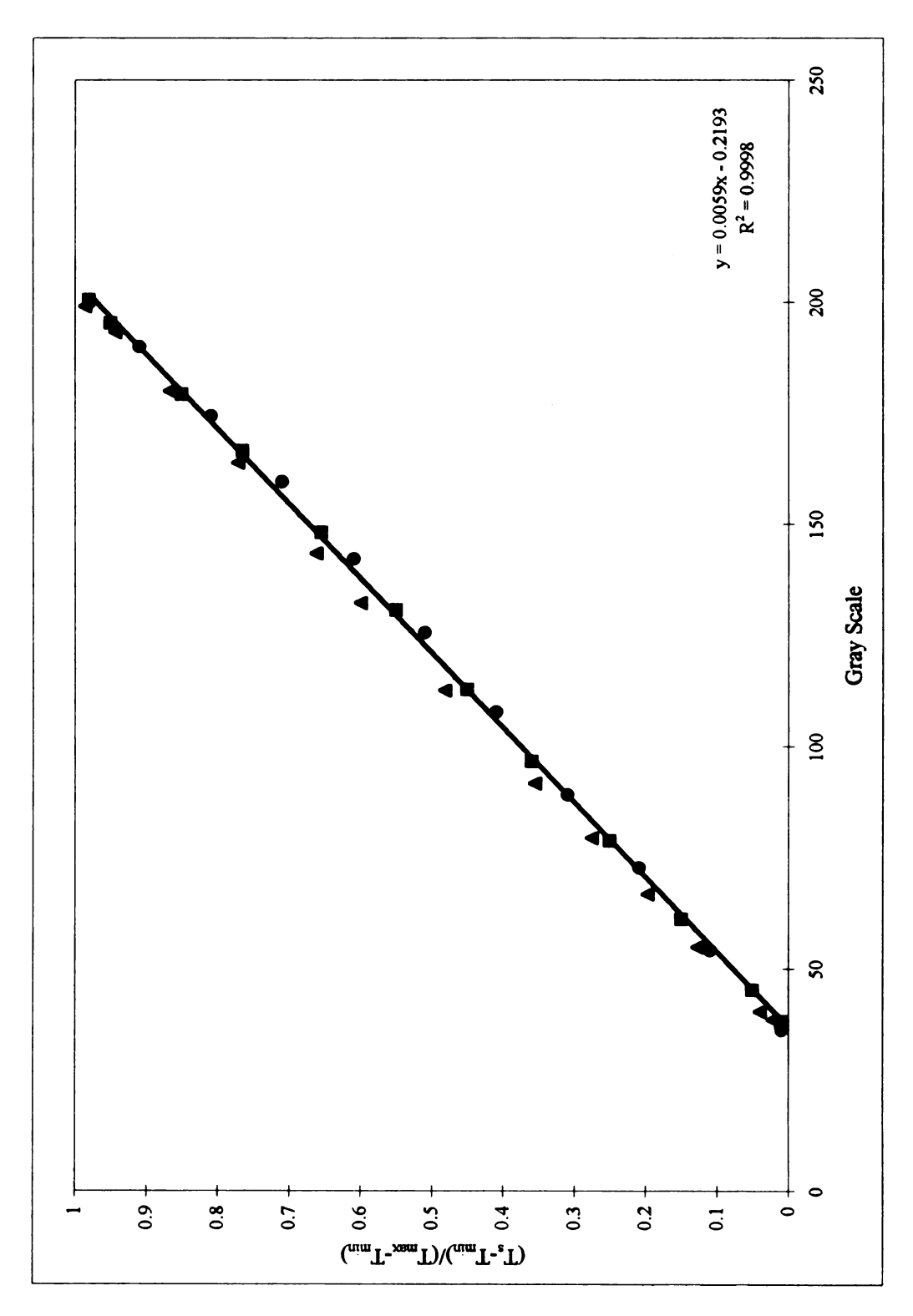


Figure B.4. Infrared camera calibration curve for the 10, 20 and 50C temperature ranges. Other imaging parameters were similar to the ones reported in Figure B.1, 2, and 3.

B.2 Calibration Data for Thermocouple Measurements

This section will present the calibration data of the thermocouples used in this study.

Table B.1 include the freezing and boiling point calibration data. These calibration points were produced as described in the experimental methodology chapter.

It can be seen that all measurements were within the manufacturer reported uncertainty of the thermocouples. The manufacturer reported uncertainty for these thermocouple was the higher of 1°C or 0.75% of the reading [Omega engineering, 1992].

Finally, Figures B.5a and B.5b show the location of the thermocouples mounted on the back side of both test sections and inside the insulation, respectively.

Table B.1 Freezing and boiling thermocouple calibration data.

Thermocouple Number	Freezing Calibration Data (°C)	Boiling Calibration Data (°C)
1	0.4	99.8
2	0.3	99.8
3	0.2	99.9
4	0.3	99.8
5	0.3	99.8
6	0.3	99.7
7	0.3	99.8
8	0.3	99.8
9	0.2	99.8
10	0.2	99.8
11	0.3	99.8
12	0.3	99.8
13	0.2	99.9
14	0.3	99.8
15	0.3	99.8
16	0.4	99.8
17	0.2	99.8
18	0.4	99.7
19	0.2	99.8
20	0.3	99.8
21	0.3	99.8
22	0.3	99.8
23	0.2	99.6
24	0.2	99.7
25	0.2	99.8
26	0.2	99.8
27	0.3	99.8
28	0.25	99.7
29	0.25	99.7
30	0.23	99.8
31	0.2	99.8
31 32		99.8
	0.2	
33		99.6
34	0.3	99.7
35	0.3	99.7
36	0.2	99.8
37	0.2	99.8
38	0.3	99.8
39	0.2	99.7
40	0.3	99.8
50	0.2	99.7
51	0.2	99.7
52	0.3	99.8
53	0.2	99.7
54	0.2	99.7
55	0.3	99.8

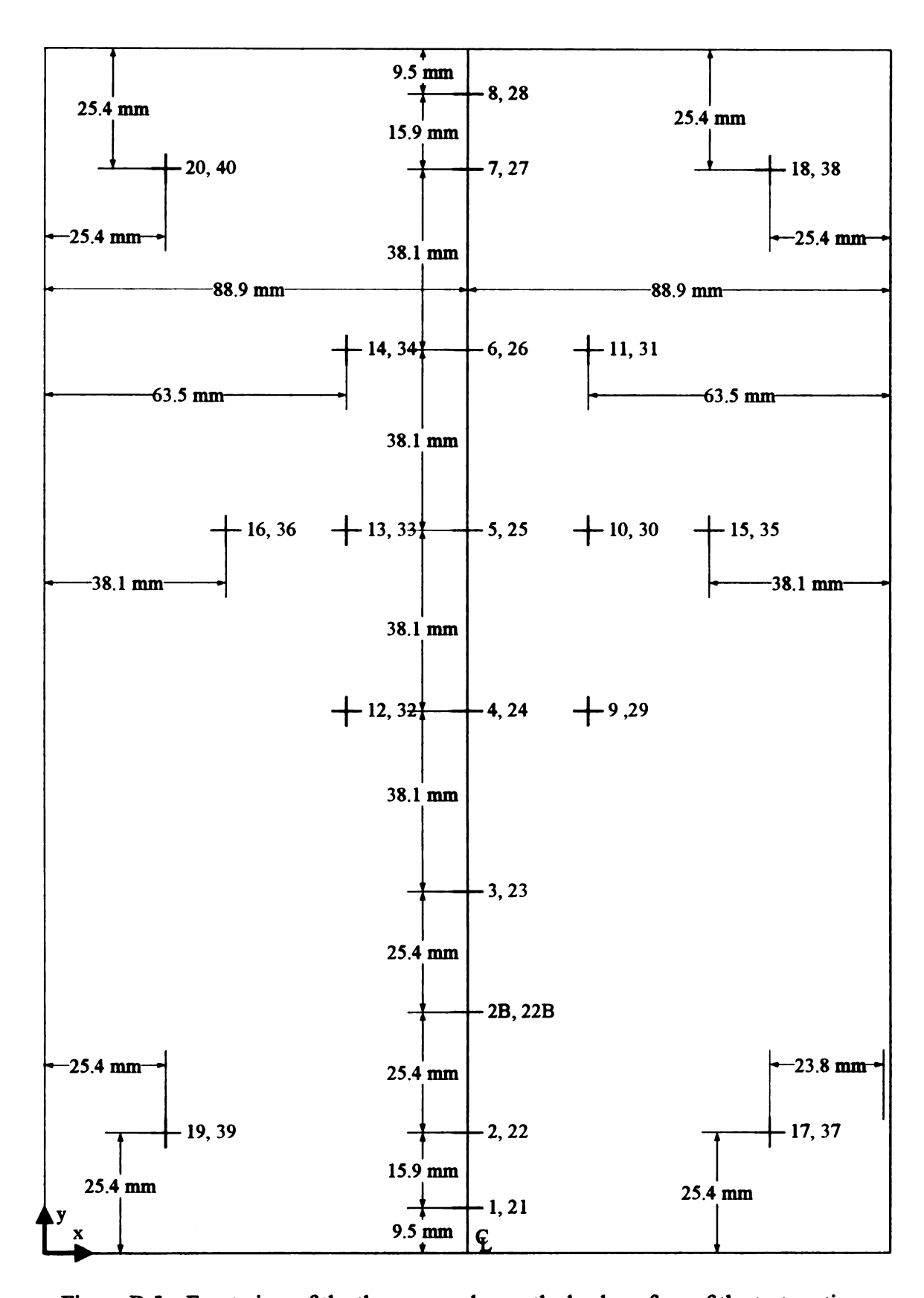


Figure B.5a. Front view of the thermocouples on the back surface of the test section.

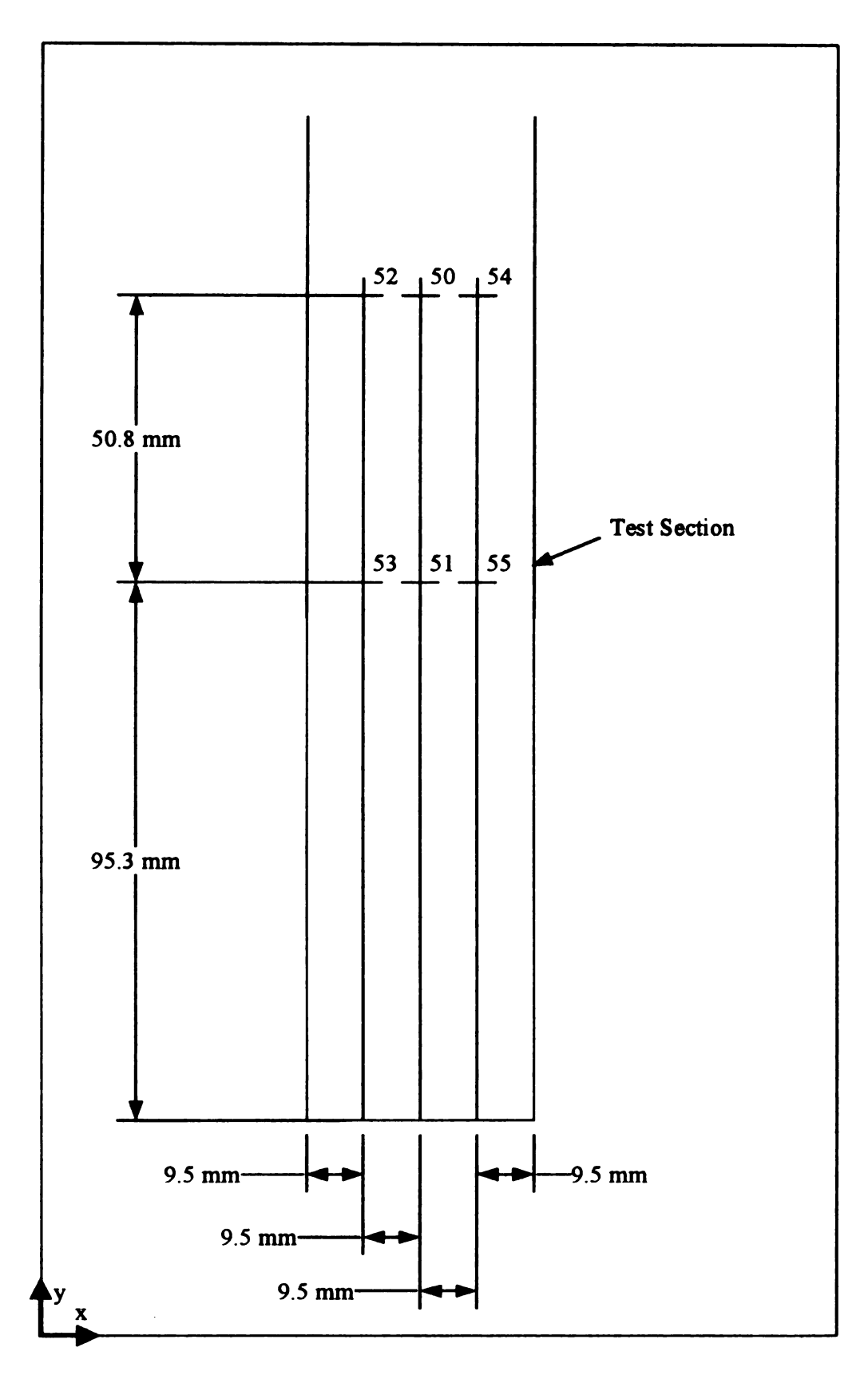


Figure B.5b. Side view of the thermocouples inside the insulation.

APPENDIX C

Uncertainty Calculations for the Local Convection Heat Transfer Coefficient for the Isoflux Boundary Condition This appendix will present and discuss the uncertainty associated will all the measurements performed in this study and their contribution to the uncertainty of the local convection heat transfer coefficient.

The local convective coefficient was calculated using a different form of Eq. 2.1 used in computing h_x :

$$h_{x} = \frac{q_{\text{total}} - q_{\text{cond}}}{(T_{s} - T_{i})A}$$
 (C.1)

The uncertainty of h_x was computed by expanding Eq. C.1 according to the propagation of error analysis shown in Eq. 3.1 [Beckwith et al., 1993, Moffat, 1988, Kline and McClintock, 1953, and ANSI/ASME Measurement Uncertainty, 1985]:

$$\Delta h = \left[\left(\frac{\partial h}{\partial q_{total}} \Delta q_{total} \right)^{2} + \left(\frac{\partial h}{\partial q_{cond}} \Delta q_{cond} \right)^{2} + \left(\frac{\partial h}{\partial T_{s}} \Delta T_{s} \right)^{2} + \left(\frac{\partial h}{\partial T_{j}} \Delta T_{j} \right)^{2} + \left(\frac{\partial h}{\partial A} \Delta A \right)^{2} \right]^{7/2}$$
(C.2)

The partial derivative of each term can be expanded and Eq. C.2 can be rearranged in the following form:

$$\Delta h = \frac{(q_{total} - q_{cond})}{(T_s - T_j)A} \left[\left(\frac{\Delta q_{total}}{q_{total} - q_{cond}} \right)^2 + \left(\frac{\Delta q_{cond}}{q_{total} - q_{cond}} \right)^2 + \left(\frac{\Delta T_s}{(T_s - T_j)} \right)^2 + \left(\frac{\Delta T_j}{(T_s - T_j)} \right)^2 + \left(\frac{\Delta A}{A} \right)^2 \right]^{\frac{1}{2}}$$
(C.3)

The following sections will discuss the method used to determine the uncertainty associated with each of the measured quantities in this experiment.

C.1 The Uncertainty of the Total Energy Term

The total electrical energy applied to the system was computed using:

$$q_{total} = I^2 R = IV (C.4)$$

where I is the electrical current applied to the test section, R is the electrical resistance of the test section, and V is the electrical voltage across the test section. The uncertainty of q_{total} was computed using Eq. C.5 [Beckwith et al., 1993]:

$$\Delta \mathbf{q} = \left[\left(\frac{\partial \mathbf{q}}{\partial \mathbf{I}} \Delta \mathbf{I} \right)^2 + \left(\frac{\partial \mathbf{q}}{\partial \mathbf{v}} \Delta \mathbf{v} \right)^2 \right]^{\frac{1}{2}}$$

$$\Delta \mathbf{q} = \mathbf{V} \Delta \mathbf{I} + \mathbf{I} \Delta \mathbf{V}$$
(C.5)

where ΔI is defined as:

$$\Delta I = \left[\left(\Delta i_{\text{resistance difference}} + \Delta i_{\text{DMM resolution}} + \Delta i_{\text{DMM precision}} \right)^2 + \left(\Delta i_{\text{bias}} \right)^2 \right]^{\frac{1}{2}}$$

where $\Delta i_{resistance}$ represented the percent difference in the electrical resistance between the two test sections. The two test sections were connected in parallel, therefore, the difference in electrical resistance resulted in a difference in the current supply to each test section. This difference was considered an error term because in the actual test, the current was measured across the two test sections combined. This term was computed using the measured test section resistance without any applied electricity. The ΔI_{DMM} resolution term represents the resolution of the digital multimeter (DMM). The ΔI_{DMM} precision term was neglected in this case because only one measurement of the DMM was recorded. The Δi_{bias} term was computed using the following relationship [Beckwith et al., 1993]:

$$\Delta i_{bias} = (0.5\% \text{ of reading} + 0.05\% \text{ of full scale of the meter})$$

The voltage uncertainty was computed using the following relationship [Beckwith et al., 1993]:

$$\Delta V = \left[\left(\Delta v_{DMM \text{ resolution}} + \Delta v_{DMM \text{ precision}} \right)^2 + \left(\Delta v_{bias} \right)^2 \right]^{\frac{1}{2}}$$

The voltage uncertainty terms were evaluated in a fashion similar to the current uncertainty terms described above. The values of the terms associated with computing the total energy uncertainty are shown in Table C.1 below.

Table C.1. Estimated uncertainty of the total energy term.

Term Symbol	Uncertainty Value	Units
I	9.40E-01	amps
ΔΙ	2.65E-02	amps
Δi _{resistance} difference	2.11E-02	amps
Δi _{DMM resolution}	1.00E-03	amps
Δi _{bias}	1.47E-02	amps
V	5.07E+01	volts
ΔV	7.54E-01	volts
ΔV _{DMM} resolution	1.00E-02	volts
Δv_{bias}	7.54E-01	volts
VΔI	1.81E+00	W
IΔV	5.01E-01	W
Gtotal	4.76E+01	W
Δq_{total}	1.52E+00	W

Table C.1 shows that the current uncertainty term ($V\Delta I$) is the dominant contributor to the total energy uncertainty term.

C.2 The Uncertainty of the Conduction Losses Term

The conduction heat losses were computed using:

$$q_{cond} = -k \frac{(T_s - T_{ins})}{y_{ins}}$$
 (C.6)

Applying the same propagation of error procedure illustrated in Eq. C.2 and C.3, the heat conduction uncertainty was computed using:

$$\Delta q_{cond} = \frac{k(T_s - T_{ins})}{y_{ins}} \left[\left(\frac{\Delta k}{k} \right)^2 + \left(\frac{\Delta T_s}{T_s - T_{ins}} \right)^2 + \left(\frac{\Delta T_{ins}}{(T_s - T_{ins})} \right)^2 + \left(\frac{\Delta y_{ins}}{y_{ins}} \right)^2 \right]^{\frac{1}{2}}$$
 (C.7)

The uncertainty in the k term was approximated. The uncertainty in the temperature terms will be discussed in the following sections. Finally, the uncertainty in the conduction distance was estimated using the resolution of the measuring tape. The values of the terms used to compute the conduction losses uncertainty are shown in Table C.2 below.

Table C.2. Estimated uncertainty of the conduction losses term.

Term Symbol	Uncertainty Value	Units
k	3.80E-02	W/m ² K
Δk	9.50E-03	W/m ² K
Tims	4.55E+01	°C
ΔT_{ins}	5.65E-01	°C
T _s	4.62E+01	°C
ΔTs	5.65E-01	°C
Yins	1.90E-02	m
Δy_{ins}	1.59E-03	m
Δk/k	6.25E-02	
$\Delta T_s/(T_s-T_{ins})$	7.45E-01	
$\Delta T_{ins}/(T_s-T_{ins})$	7.45E-01	
Δy _{ins} /y _{ins}	8.14E-03	
Goond	1.41E+00	W
Δq_{cond}	1.77E+00	W

The calculations in Table C.2 show that the uncertainty of the thermocouple measurements in determining the surface and insulation temperatures were the main contributor to the uncertainty of the conduction losses term.

C.3 The Uncertainty of the Surface Temperature Term

The surface temperature uncertainty was computed for both infrared and thermocouple measurements using:

$$\Delta T_{s} = \left[\left(\Delta T_{\text{precision}} \right)^{2} + \left(\Delta T_{\text{bias}} \right)^{2} \right]^{\frac{1}{2}} \tag{C.8}$$

C.3.1 Infrared Imaging

The precision error associated with the infrared imaging measurement was computed using the resolution of the infrared camera and the student's t-distribution [Beckwith et al., 1993]:

$$\Delta T_{s_{R, precision}} = t - \frac{S}{\sqrt{n}} + \Delta T_{s_{R, resolution}}$$
 (C.9)

The student's t-distribution was used to calculate the probability distribution for a small sample of data assuming that the population satisfied a Gaussian (Normal) distribution. The t-distribution is available in the literature for a given sample size, n, and confidence level. The standard deviation, S, was determined using actual measurements of the same point under steady state conditions. The student's t-distribution method was used to compute the temperature uncertainty in term of the gray scale intensity. Then the infrared camera calibration curve was used to determine the uncertainty value in terms of the

temperature. The $\Delta T_{s, resolution}$ was computed based on the resolution of the infrared camera [Inframetrics, 1988].

The bias uncertainty was estimated based on the noise level of the camera as reported by the manufacturer [Inframetrics, 1988]. The values of the terms associated with using the IR camera to determine the surface temperature uncertainty are shown in Table C.3

Table C.3. Estimated uncertainty of the surface temperature using infrared camera measurements.

Term Symbol	Uncertainty Value	Units
T _{s IR}	4.51E+01	°C
$\Delta T_{s IR}$	3.20E-01	°C
ΔT _{s IR, precision}	1.25E-02	°C
$t S/(n)^{1/2}$	1.20E-02	°C
ΔT _{s IR, resolution}	1.00E-01	°C
ΔT _{s IR, bias}	9.00E-02	°C

The infrared camera bias uncertainty was the major contributor to the surface temperature uncertainty when determined using the IR camera measurements.

C.3.2 Thermocouple Measurements

The precision error associated with thermocouple measurements was computed using the resolution of the A/D data acquisition board and the student's t-distribution [Beckwith et al., 1993]:

$$\Delta T_{s_TC, precision} = t - \frac{S}{\sqrt{n}} + \Delta T_{A/D \text{ board resolution}}$$
 (C.10)

The student's t-distribution term was evaluated similarly to the procedure outlined in section C.3.1. The $\Delta T_{A/D \, board \, resolution}$ term was evaluated using the manufacturer reported values [Keithley Instruments].

The thermocouple bias uncertainty was computed using:

$$\Delta T_{s TC, bias} = \Delta T_{TC bias} + \Delta T_{A/D board bias}$$
 (C.11)

The thermocouple bias terms were obtained from the manufacturers catalog [Omega Engineering, 1992 and Keithley Instruments]. The values of the terms associated with computing the surface temperature uncertainty using thermocouple measurements are shown in Table C.4.

Table C.4. Estimated uncertainty of the surface temperature using thermocouple measurements.

Term Symbol	Uncertainty Value	Units
T _{s TC}	4.62E+01	°C
ΔT _{s TC}	5.65E-01	°C
ΔT _{s TC, precision}	6.01E-03	°C
t S/(n) ^{1/2}	3.75E-02	°C
ΔT _{A/D resolution}	4.00E-02	°C
ΔT _{TC bias}	3.14E-01	°C
ΔT _{s TC, bias}	4.00E-01	°C
ΔT _{A/D bias}	1.60E-01	°C

Table C.4 shows that the thermocouple bias uncertainty was the dominant contributor to the surface temperature uncertainty when determined using thermocouple measurements.

C.4 The Uncertainty of the Jet Temperature Term

The jet temperature was measured using thermocouples inserted in the plenum.

Therefore, the uncertainty of this term was similar to the surface temperature uncertainty outlined in section C.3.2. A representative value of the jet temperature was 21.8°C.

C.5 The Uncertainty of the Surface Area Term

The surface area uncertainty was computed using:

$$\Delta A = \left[\left(\frac{\partial A}{\partial w} \Delta w \right)^2 + \left(\frac{\partial A}{\partial L} \Delta L \right)^2 \right]^{\frac{1}{2}}$$

$$\Delta A = \left[(L \Delta w)^2 + (w \Delta L)^2 \right]^{\frac{1}{2}}$$
(C.12)

where L and w are the length and the width of the test section, respectively. The uncertainty of both terms was determined from the resolution of the measurement devices [Beckwith et al., 1993]. The values of the terms used to compute the area uncertainty are shown in Table C.5.

Table C.5. Estimated uncertainty of the test section surface area.

Term Symbol	Uncertainty Value	Units
L	2.53E-01	m
ΔL	1.00E-03	m
w	1.80E-01	m
Δw	1.00E-03	m
LΔw	6.40E-08	m²
wΔL	3.24E-08	m²
A	4.55E-02	m²
ΔΑ	3.10E-04	m²

The length and width uncertainty terms contributed equally to the area uncertainty term.

In general, the area uncertainty term was negligible in comparison to the other terms discussed earlier.

APPENDIX D

Infrared Images of the Surface Temperature Distribution for the Isoflux Boundary Condition

This appendix include thermal images from four different tests. The tests were conducted using the same average velocity value and energy supplied to the test section. Figures D.1-D.4 demonstrate the reproducibility of the experimental procedure used in this study.

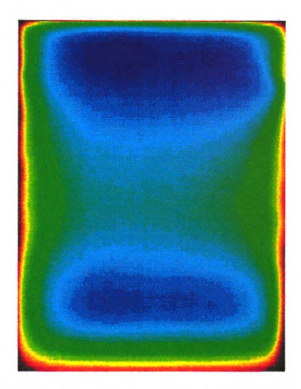


Figure D.1. 2-D infrared surface temperature profile from test number a with $q^{*}_{conv} = 1023 \ W/m^2$ and $u_{ref} = 10 \ m/s$.

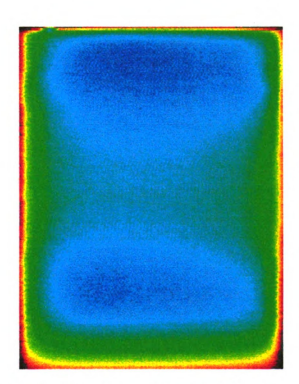


Figure D.2. 2-D infrared surface temperature profile from test number c with $q^{"}_{conv} = 1023 \text{ W/m}^2$ and $u_{ref} = 10 \text{ m/s}$.

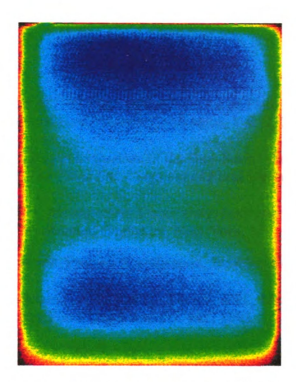


Figure D.3. 2-D infrared surface temperature profile from test number d with $q^n_{conv} = 1023 \text{ W/m}^2$ and $u_{ref} = 10 \text{ m/s}$.

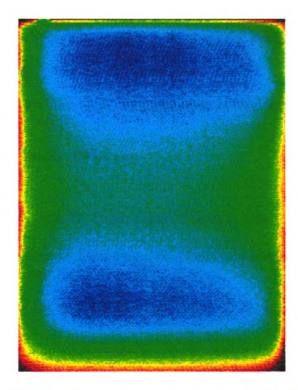


Figure D.4. 2-D infrared surface temperature profile from test number e with $q^u_{conv}=1023\ W/m^2$ and $u_{ref}=10\ m/s.$

LIST OF REFERENCES

- 1. Akfirat, J. C., Transfer of Heat From an Isothermal Flat Plate to a Two-dimensional Wall Jet, 3rd International Heat Transfer Conference, Vol. 2, 274-279, 1966.
- 2. Ali, S. K. and Foss, J. F., An Evaluation of the Biot-Savart Computational Model for A Slit-Jet Flow Field, *The Third Intl. Congress of Fluid Mechanics*, 1990.
- 3. ANSI/ASME PTC 19.1, Measurement Uncertainty: Instruments and Apparatus, *The American Society of Mechanical Engineers*, New York, NY, 1985.
- 4. Applied Films Corporation, Product Specification, Boulder, CO, 1993.
- 5. Beckwith, T. G., Marangoni, R. D. and Lienhard V, J. H., Mechanical Measurements, 5th ed., Addison-Wesley Publishing Company, Inc., 1993.
- 6. Chase Products Co., Maywood, IL.
- 7. Ciba-Geigy Tooling, East Lansing, MI.
- 8. Dynaloy, Inc., Product Specifications, Hanover, NJ.
- 9. FOR.A Company Limited, Japan.
- 10. Foss, J. F., Turbulent Shear Flow Laboratory, unofficial publication, 1996
- 11. Hewlett Packard Corp.
- 12. Incropera, F. P., and DeWitt, D. P., Fundamentals of Heat and Mass Transfer, 3rd ed., John Wiley & Sons, 1990.
- 13. Inframetrics, User Manual, 1988.
- 14. JVC Co. Japan.
- 15. Keithley Instruments, DAS-TC User's Guide, Taunton, MA.
- 16. Kline, S. J., and McClintock, Describing Uncertainties in Single-Sample Experiments, *Mechanical Engineering Journal of ASME*, 1953.
- 17. Launder, B. E., and Rodi, W., The Turbulent Wall Jet, *Prog. Aerospace Sci.*, 19, 81-128, 1981.
- 18. Mabuchi, I. and Kumada, M., Studies on Heat Transfer to Turbulent Jets with Adjacent Boundaries, *Bulletin JSME*, 15 (88), 1236-1245, 1972.
- 19. Media Cybernetics, Silver Spring, MD.

- 20. MKS Instruments, Inc., User Manual for Baratron Pressure Transducer, Andover, MA.
- 21. Moffat, R. J., Describing the Uncertainties in Experimental Results, Experimental *Thermal and Fluid Science*, 1, 3-17, 1988.
- 22. Nizou, P. Y., Heat and Momentum Transfer in a Plane Turbulent Wall Jet, ASME J. Heat Trans., 103, 138-140, 1981.
- 23. Omega, The Temperature Handbook, 1992.
- 24. Panasonic Co., Japan.
- 25. Panton, L. P., Incompressible Flow, Wiley Interscience, 1984.
- 26. Sigalla, A., Experimental Data on Turbulent Wall Jets, Aircraft Engineering, 33, 131-134, 1958.
- 27. Willenborg, K., Investigation of the Velocity and Temperature Fields of a Model Defroster Flow, M.S. Thesis, Mechanical Engineering Dept., Michigan State University, East Lansing, MI, 1996.